

Momentum-Net: Fast and convergent iterative neural network for inverse problems

Il Yong Chun, *Member, IEEE*, Zhengyu Huang*, Hongki Lim*, *Student Member, IEEE*,
and Jeffrey A. Fessler, *Fellow, IEEE*

Abstract—Iterative neural networks (INN) are rapidly gaining attention for solving inverse problems in imaging, image processing, and computer vision. INNs combine regression NNs and an iterative model-based image reconstruction (MBIR) algorithm, leading to both good generalization capability and outperforming reconstruction quality over existing MBIR optimization models. This paper proposes the first fast and convergent INN architecture, *Momentum-Net*, by generalizing a block-wise MBIR algorithm that uses momentums and majorizers with regression NNs. For fast MBIR, Momentum-Net uses *momentum* terms in extrapolation modules, and noniterative MBIR modules at each layer by using *majorizers*, where each layer of Momentum-Net consists of three core modules: image refining, extrapolation, and MBIR. Momentum-Net guarantees convergence to a fixed-point for general differentiable (non)convex MBIR functions (or data-fit terms) and convex feasible sets, under two asymptomatic conditions. To consider data-fit variations across training and testing samples, we also propose a regularization parameter selection scheme based on the spectral radius of majorization matrices. Numerical experiments for light-field photography using a focal stack and sparse-view computational tomography demonstrate that given identical regression NN architectures, Momentum-Net significantly improves MBIR speed and accuracy over several existing INNs; it significantly improves reconstruction quality compared to a state-of-the-art MBIR method in each application.

Index Terms—Iterative neural network, deep learning, model-based image reconstruction, inverse problems, block proximal extrapolated gradient method, block coordinate descent method, light-field photography, X-ray computational tomography.

1 INTRODUCTION

DEEP regression neural network (NN) methods have been actively studied for solving diverse inverse problems, due to their effectiveness at mapping noisy signals into clean signals. Examples include image denoising [1]–[4], image deconvolution [5], [6], image super-resolution [7], [8], magnetic resonance imaging (MRI) [9], [10], X-ray computational tomography (CT) [11]–[13], and light-field (LF) photography [14], [15]; see references in [16] for medical imaging applications. However, having a greater mapping capability (i.e., higher the NN complexity) can increase the overfitting risks [17]–[19]. An alternative approach to solving inverse problems is a so-called *iterative NN* (INN) that combines regression NNs – called “refiners” or denoisers – with an unrolled iterative model-based iterative reconstruction (MBIR) algorithm [20]–[27]. This alternative approach can regulate overfitting of regression NNs, by balancing physical data-fit of MBIR and prior information estimated by refining NNs [17], [19]. This “soft-refiner” approach has been successfully applied to several extreme imaging systems, e.g., highly undersampled MRI [20], [25],

[28]–[30], sparse-view CT [24], [27], [31], low-count positron emission tomography [19], [32], [33], and single photon emission computed tomography [34].

1.1 From block-wise optimization to INN

To recover signals $x \in \mathbb{C}^N$ from measurements $y \in \mathbb{C}^m$, consider the following MBIR optimization problem (Appendix A provides mathematical notations):

$$\underset{x \in \mathcal{X}}{\operatorname{argmin}} F(x; y, z), \quad F(x; y, z) := f(x; y) + \frac{\gamma}{2} \|x - z\|_2^2, \quad (\text{P0})$$

where \mathcal{X} is a set of feasible points, $f(x; y)$ is data-fit function that measures deviations of model-based predictions of x from data y , considering models of imaging physics (or image formation) and noise statistics in y , γ is a regularization parameter, and $z \in \mathbb{C}^N$ is some high-quality approximation to the true unknown signal x . In (P0), the signal recovery accuracy increases as the quality of z improves [18, Prop. 3]; however, it is difficult to obtain such z in practice. Alternatively, there has been a growing trend in learning sparsifying regularizers (e.g., convolutional regularizers [24], [35]–[37]) from training datasets and applying the trained regularizers to the following block-wise MBIR problem: $\underset{x \in \mathcal{X}}{\operatorname{argmin}} f(x; y) + \min_{\zeta} r(x, \zeta; \mathcal{O})$, where a learned regularizer $\min_{\zeta} r(x, \zeta; \mathcal{O})$ quantifies consistency between x and refined sparse signal ζ via some learned operators \mathcal{O} . Recently, we have constructed INNs by generalizing the corresponding block-wise MBIR updates with regression NNs [25], [27]; see the proposed generalization in §2.1–2.2. In existing INNs, two major challenges exist: convergence and acceleration.

- The authors indicated by asterisks (*) contributed equally to this work.
- This work is supported in part by the Keck Foundation, NIH U01 EB018753, NIH R01 EB023618, and NIH R01 EB022075.
- Il Yong Chun, Zhengyu Huang, Hongki Lim, and Jeffrey A. Fessler are with the Department of Electrical Engineering and Computer Science, The University of Michigan, Ann Arbor, MI 48019 USA (email: iychun@umich.edu; zyhuang@umich.edu; hongki@umich.edu; fessler@umich.edu).
- This paper has supplementary material. The prefix “S” indicates the numbers in section, theorem, equation, figure, table, and footnote in the supplementary material.
- This paper was presented in part at the Allerton Conference on Communication, Control, and Computing, Monticello, IL, USA, in Oct. 2018.

1.2 Challenges in existing INNs: Convergence

First, existing convergence analysis has some practical limitations. The original form of plug-and-play (PnP [23], [38]–[40]) is motivated by the alternating direction method of multipliers (ADMM [41]), and its fixed-point convergence has been recently analyzed with consensus equilibrium perspectives [23]. However, similar to ADMM, its practical convergence guarantee largely depends on how one selects ADMM penalty parameters. For example, [22], [42] reported unstable convergence behaviors of PnP-ADMM with fixed ADMM parameters. To moderate this problem, [40] proposed a scheme that adaptively controls the ADMM parameters based on relative residuals. However, similar to the residual balancing technique [41, §3.4.1], the scheme in [40] requires tuning initial parameters. Regularization by Denoising (RED [22]) is an alternative that moderates some limitations (including the difficulty of tuning ADMM parameters) of PnP frameworks. In particular, RED aims to make a clear connection between optimization and a denoiser \mathcal{D} , by defining its prior term by (scaled) $x^T(x - \mathcal{D}(x))$. Nonetheless, [42] showed that many practical denoisers do not satisfy the Jacobian symmetry in [22], and proposed a less restrictive method, score-matching by denoising.

The convergence analysis of INN inspired by the relaxed projected gradient descent (RPGD) method in [31] has the least restrictive conditions on the regression NN among the existing INNs. This method replaces a projector of a projected gradient descent method that solves constrained least-squares problem, with an image refining NN. However, the RPGD-inspired INN directly applies an image refining NN to gradient descent updates of data-fit; thus, this INN relies heavily on the mapping performance of a refining NN and can have overfitting risks (similar to non-MBIR regression NNs, e.g., FBPCNN [12]). In addition, it exploits the data-fit term only for the first few iterations; see its relaxation parameter behavior in [31, Fig. 5(c)]. We refer the perspective used in RPGD-inspired INN and its related works [26], [43] as “hard-refiner”: different from soft-refiners, these methods do not use a refining NN as a regularizer. More recently, [26] presented convergence analysis for INN inspired by proximal gradient descent method. However, their analysis is based on noiseless measurements, and this condition is too strict in most practical applications.

Broadly speaking, existing convergence analysis largely depends on the (firmly) nonexpansive property of image refining NNs [22], [23], [42], [31, PGD], [26]. However, except for a single-layer convolutional autoencoding NN, it is unclear whether trained image refining NNs satisfy the non-expansiveness in practice [27]. To guarantee convergence of INNs even when using possibly *expansive* image refining NNs, we proposed a method that normalizes the output signal of image refining NNs by their Lipschitz constants [27]. However, if one uses expansive NNs that are identical across iterations, it is difficult to obtain “best” image recovery with that normalization scheme. In addition, there does not yet exist theoretical convergence results when refining NNs change across iterations, yet iteration-wise refining NNs are widely studied [20], [21], [25], [28]. Finally, existing analysis considers only a narrow class of data-fit terms: most analyses consider a quadratic function with a

linear imaging model [26], [31] or more generally, a convex cost function [23], [42] that should be minimized with a practical closed-form solution. No theoretical convergence results exist for *general* (non)convex data-fit terms, iteration-wise NN denoisers, and a general set of feasible points.

1.3 Challenges in existing INNs: Acceleration

Compared to non-MBIR regression NNs that do not exploit data-fit $f(x; y)$ in (P0), INNs require more computation because such methods additionally consider the imaging physics or image formation models. In particular, computational complexities increase as the imaging system or image formation model becomes larger-scale, e.g., LF photography from a focal stack, 3D CT, parallel MRI using many receive coils, and image super-resolution. Thus, acceleration becomes a critical issue in INNs. First, consider the existing methods motivated by ADMM or block coordinate descent (BCD) method: examples include PnP [23], [40], RED [22], [42], MoDL [30], BCD-Net [17], [19], [25], etc. These methods can require multiple inner iterations to balance data-fit and prior information estimated by trained refining NNs, increasing total MBIR time. For example, in solving such problems, each outer iteration involves $x^{(i+1)} = \operatorname{argmin}_x F(x; y, z^{(i+1)})$, where $F(x; y, z^{(i+1)})$ is given as in (P0) and $z^{(i+1)}$ is the output from the i th image refining NN (possibly identical across iterations i). For LF imaging system using focal stack data, solving the above problem requires multiple iterations, and the total computational cost scale with the numbers of photosensors and sub-aperture images; see details in §4.1.2. In addition, when the data-fit term $f(x; y)$ is nonconvex, convergence guarantees of these methods can break, because in general, the proximal mapping $\operatorname{argmin}_x f(x; y) + \gamma \|x - z^{(i+1)}\|_2^2$ is no longer nonexpansive (see the proof of Proposition 14) and the corresponding algorithm can be trapped at a local minimum even with many inner iterations. Second, consider existing works motivated by (proximal or projected) gradient descent methods [21], [26], [28], [31]. These methods resolve the aforementioned issue of the first INN class motivated by ADMM or BCD; however, there exists no sophisticated step-size control or backtracking scheme for them. Most importantly, considering that accelerated proximal gradient (APG) methods using *momentum* terms can significantly accelerate convergence rates for solving composite convex problems [44], [45], we expect that the methods in the second class have yet to be maximally accelerated. The work in [43] applied PnP to the accelerated proximal gradient method [45]. However, similar to RPGD [31], it is a hard-refiner method using some state-of-the-art denoisers (e.g., BM3D [46]) but not trained NNs; there exists no convergence behavior analysis; it does not aim for fast MBIR.

1.4 Contributions and organization of the paper

This paper proposes *Momentum-Net*, the first INN architecture that aims for fast and convergent MBIR. The architecture of Momentum-Net is motivated by applying the Block Proximal Extrapolated Gradient method using a Majorizer (BPEG-M) [24], [35] to MBIR using trained convolutional autoencoders [24], [25], [37]. Specifically, each layer (or

iteration) of Momentum-Net consists of three core modules: image refining, extrapolation, and MBIR. For fast MBIR, Momentum-Net uses *momentum* terms, i.e., information from previous differences to amplify the changes in subsequent iterations, in extrapolation modules, and *noniterative* MBIR modules at each layer. In addition, Momentum-Net resolves the convergence issues aforementioned in §1.2: for general differentiable (non)convex data-fit terms and convex feasible sets, it guarantees convergence to a point that satisfies fixed-point and critical point conditions, under some mild conditions and two asymptotic conditions, i.e., *asymptotically nonexpansive paired refining NNs* and *asymptotically block-coordinate minimizer*.

The remainder of this paper is organized as follows. §2 constructs the Momentum-Net architecture motivated by BPEG-M algorithm that solves MBIR problem using learned convolutional regularizer, describes its relation to existing works, and analyzes its convergence to a point that satisfies critical point and fixed-point conditions under some reasonable assumptions. §3 provides details of training INN, including residual convolutional autoencoder architecture, training loss function, and related properties, and proposes a regularization parameter selection scheme to consider data-fit variations across training and testing samples. §4 considers two extreme imaging applications: sparse-view CT and LF photography using a focal stack. §4 reports numerical experiments of both the applications that the proposed Momentum-Net using extrapolation significantly improves MBIR speed and accuracy, over the existing (soft-refiner) INNs [21]–[23], [25], [28], [30] that correspond to BCD-Net [25] or Momentum-Net using *no extrapolation*. Furthermore, §4 reports sparse-view CT experiments that show Momentum-Net significantly improves reconstruction quality compared to the state-of-the-art MBIR method using learned convolutional regularizer [24], [37]; §4 reports LF photography experiments that show Momentum-Net significantly improves qualities of LF reconstruction and depth estimation, compared to the state-of-the-art MBIR method using 4D edge-preserving (EP) regularizer [47]. Finally, Appendix B analyzes the sequence convergence of BCD-Net [25], and describes the convergence benefits of Momentum-Net over BCD-Net.

2 MOMENTUM-NET: WHERE BPEG-M MEETS NNS FOR INVERSE PROBLEMS

2.1 Motivation: BPEG-M algorithm for MBIR using learned convolutional regularizer

Consider the following block multi-(non)convex problem for recovering signal x from measurements y [24], [37] (see the setup of block multi-(non)convex problems in §S.1.1):

$$\begin{aligned} \argmin_{x \in \mathcal{X}} f(x; y) + \gamma \left(\min_{\{\zeta_k\}} r(x, \{\zeta_k\}; \{h_k\}) \right), \\ r(x, \{\zeta_k\}; \{h_k\}) := \sum_{k=1}^K \frac{1}{2} \|h_k * x - \zeta_k\|_2^2 + \beta_k \|\zeta_k\|_1, \end{aligned} \quad (1)$$

where \mathcal{X} is a closed set, $f(x; y) + \gamma r(x, \{\zeta_k\}; \{h_k\})$ is a (continuously) differentiable (non)convex function, $\min_{\{\zeta_k\}} r(x, \{\zeta_k\}; \{h_k\})$ is a learned convolutional regularizer [24], [36], $\{\zeta_k : k = 1, \dots, K\}$ is a set of sparse

features that correspond to refined versions of $\{h_k * x\}$, $\{h_k \in \mathbb{C}^R : k = 1, \dots, K\}$ is a set of trained filters, and R and K is the size and number of trained filters, respectively.

For solving (1) that can be viewed as two-block (i.e., x and $\{\zeta_k\}$) optimization problem, one can apply BPEG-M [24], [35], the state-of-the-art optimization framework for rapidly solving a wide range of block optimization problems with sufficiently sharp majorizers. The key ideas of BPEG-M are as follows (see BPEG-M reviews in §S.1):

- M -Lipschitz continuity – a more general concept than the classical Lipschitz continuity – for the gradient of the b th block optimization problem, $\forall b$:

Definition 1 (M -Lipschitz continuity [24]). *A function $g : \mathbb{R}^n \rightarrow \mathbb{R}^n$ is M -Lipschitz continuous on \mathbb{R}^n if there exist a (symmetric) positive definite matrix M such that*

$$\|g(u) - g(v)\|_{M^{-1}} \leq \|u - v\|_M, \quad \forall u, v \in \mathbb{R}^n.$$

- A sharper majorization matrix M that gives a tighter bound in Definition 1 leads to a tighter quadratic majorization bound in the following lemma:

Lemma 2 (Quadratic majorization via M -Lipschitz continuous gradients [24]). *Let $f(u) : \mathbb{R}^n \rightarrow \mathbb{R}$. If ∇f is M -Lipschitz continuous, then*

$$f(u) \leq f(v) + \langle \nabla_u f(v), u - v \rangle + \frac{1}{2} \|u - v\|_M^2, \quad \forall u, v \in \mathbb{R}^n.$$

Having tighter majorization bounds, sharper majorization matrices tend to accelerate BPEG-M convergence.

- The majorized block problems are “proximable”, i.e., proximal mapping of majorized function is easily computable, where the proximal mapping operator is defined by

$$\text{Prox}_r^M(z) := \argmin_u \frac{1}{2} \|u - z\|_M^2 + r(u). \quad (2)$$

- Block-wise extrapolation and momentum terms accelerate solving block multi-convex problems.

Suppose that 1) gradient of $f(x; y) + \gamma r(x, \{\zeta_k\}; \{h_k\})$ is M -Lipschitz continuous at the extrapolated point $\hat{x}^{(i+1)}$, $\forall i$; 2) trained filters in (1) satisfy the tight-frame (TF) condition, $\sum_{k=1}^K \|h_k * u\|_2^2 = \|u\|_2^2$, $\forall u$, for some boundary conditions [24]. Applying the BPEG-M framework (see Algorithm S.1) to solving (1) leads to the following block updates:

$$z^{(i+1)} = \sum_{k=1}^K \text{flip}(h_k^*) * \mathcal{T}_{\beta_k}(h_k * x^{(i)}), \quad (3)$$

$$\hat{x}^{(i+1)} = x^{(i)} + E^{(i+1)}(x^{(i)} - x^{(i-1)}), \quad (4)$$

$$x^{(i+1)} = \text{Prox}_{\mathbb{I}_{\mathcal{X}}}^{\widetilde{M}^{(i+1)}} \left(\hat{x}^{(i+1)} - (\widetilde{M}^{(i+1)})^{-1} \nabla F(\hat{x}^{(i+1)}; y, z^{(i+1)}) \right), \quad (5)$$

where $E^{(i+1)}$ is an extrapolation matrix that is updated to satisfy (8) or (9) below, $\widetilde{M}^{(i+1)}$ is a (scaled) majorization matrix for $\nabla F(x; y, z^{(i+1)})$ that is given in (7) below, $\forall i$, the proximal operator $\text{Prox}_{\mathbb{I}_{\mathcal{X}}}^{\widetilde{M}^{(i+1)}}(\cdot)$ in (5) is given by (2), and $\mathbb{I}_{\mathcal{X}}(x)$ is the indicator function of sets \mathcal{X} (i.e., $\mathbb{I}_{\mathcal{X}}$ equals to 0 if $x \in \mathcal{X}$, and ∞ otherwise). Proximal mapping update (3) has a *convolutional autoencoder* architecture that consists of encoding convolution, nonlinear thresholding, and decoding

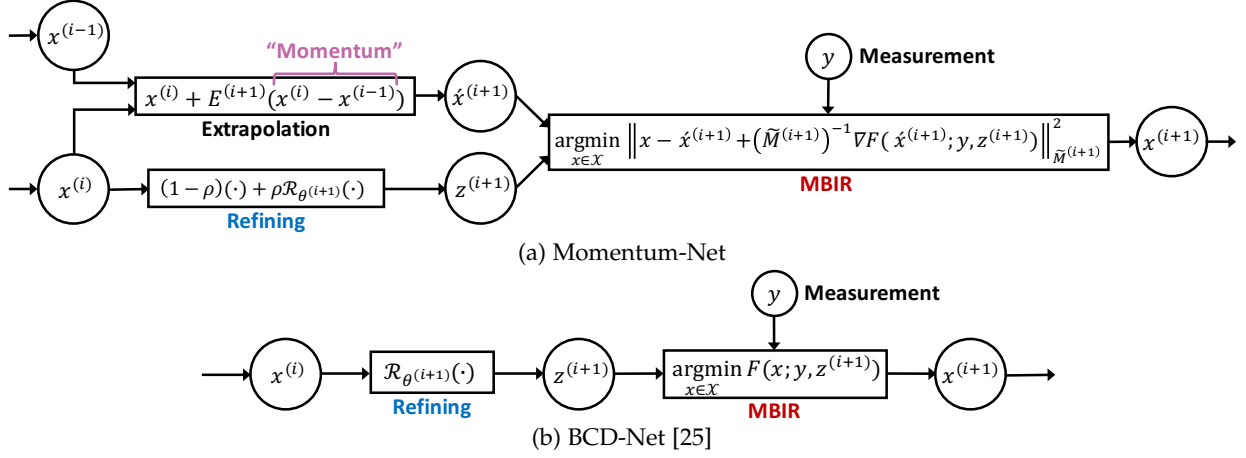


Fig. 1. Architectures of different INNs for MBIR. (a–b) The architectures of Momentum-Net and BCD-Net [25] are constructed by generalizing BPEG-M and BCD algorithms that solve MBIR problem using a convolutional regularizer trained via *convolutional analysis operator learning* (CAOL) [24], [36], respectively. (a) Removing extrapolation modules (i.e., setting the extrapolation matrices $\{E^{(i+1)} : \forall i\}$ as a zero matrix), Momentum-Net specializes to the existing gradient-descent-inspired INNs [21], [28]. When the MBIR cost function $F(x; y, z^{(i+1)})$ in (P1) has a sharp majorizer $\tilde{M}^{(i+1)}$, $\forall i$, Momentum-Net (using $\rho \approx 1$) specializes to BCD-Net; see Examples 5–6. (b) BCD-Net is a general version of the existing INNs in [20], [22], [23], [30], [38]–[40] by using layer-wise image refining NNs, i.e., $\{\mathcal{R}_{\theta^{(i+1)}} : \forall i\}$, or considering general convex data-fit $f(x; y)$.

convolution, where $\text{flip}(\cdot)$ flips a filter along each dimension, and the soft-thresholding operator $\mathcal{T}_\alpha(u) : \mathbb{C}^N \rightarrow \mathbb{C}^N$ is defined by

$$(\mathcal{T}_\alpha(u))_n := \begin{cases} u_n - \alpha \cdot \text{sign}(u_n), & |u_n| > \alpha, \\ 0, & \text{otherwise,} \end{cases} \quad (6)$$

for $n = 1, \dots, N$, in which $\text{sign}(\cdot)$ is the sign function. See details of deriving BPEG-M updates (3)–(5) in §S.1.4. The BPEG-M updates in (3)–(5) guarantee convergence to a critical point, when MBIR problem (1) satisfies some mild conditions, e.g., lower-boundedness and existence of critical points; see Assumption S.1 in §S.1.3.

The following section generalizes the BPEG-M updates in (3)–(5) and constructs the Momentum-Net architecture.

2.2 Architecture

This section establishes the INN architecture of *Momentum-Net* by generalizing BPEG-M updates (3)–(5) that solve (1). Specifically, we replace the proximal mapping in (3), $\sum_{k=1}^K \text{flip}(h_k^*) * \mathcal{T}_{\beta_k}(h_k * (\cdot))$, with a general image refining NN, $\mathcal{R}_\theta(\cdot)$, that is not necessarily written as a form of proximal operators (2), where θ denotes the vector of parameters of \mathcal{R}_θ . To effectively remove layer-wise (or iteration-wise) artifacts and give “best” signal estimates at each layer, we further generalize a refining NN $\mathcal{R}_\theta(\cdot)$ to *layer-wise* image refining NNs $\{\mathcal{R}_{\theta^{(i+1)}}(\cdot) : i = 0, \dots, N_{\text{lyr}} - 1\}$, where $\theta^{(i+1)}$ denotes the parameters for the i th layer refining NN $\mathcal{R}_{\theta^{(i+1)}}$, and N_{lyr} is the number of Momentum-Net layers. The layer-wise NNs are particularly useful for reducing overfitting risks in regression, because $\mathcal{R}_{\theta^{(i+1)}}$ is responsible for removing noise features only at the i th layer, and thus one does not need to greatly increase dimensions of its parameter $\theta^{(i+1)}$ [17], [19]. In low-dose CT reconstruction, for example, the refining NNs at the early and later layers remove streak artifacts and Gaussian-like noise, respectively [17].

Each layer of Momentum-Net consists of 1) image refining, 2) extrapolation, and 3) MBIR modules, corresponding to the BPEG-M updates (3), (4), and (5), respectively. See the architecture of Momentum-Net in Fig. 1(a) and Algorithm 1.

Algorithm 1 Momentum-Net

Require: $\{\mathcal{R}_{\theta^{(i)}}, \kappa^{(i)} : i = 1, \dots, N_{\text{lyr}}\}$, $\rho \in (0, 1)$, $\gamma > 0$, $x^{(0)} = x^{(-1)}$, y

for $i = 0, \dots, N_{\text{lyr}} - 1$ **do**

Calculate $\tilde{M}^{(i+1)}$ by (7), and $E^{(i+1)}$ by (8) or (9)

Image refining:

$z^{(i+1)} = (1 - \rho)x^{(i)} + \rho\mathcal{R}_{\theta^{(i+1)}}(x^{(i)})$ (Alg.1.1)

Extrapolation:

$\hat{x}^{(i+1)} = x^{(i)} + E^{(i+1)}(x^{(i)} - x^{(i-1)})$ (Alg.1.2)

MBIR:

$x^{(i+1)} = \text{Prox}_{\mathbb{I}_X}^{\tilde{M}^{(i+1)}}(\hat{x}^{(i+1)} - (\tilde{M}^{(i+1)})^{-1} \nabla F(\hat{x}^{(i+1)}; y, z^{(i+1)}))$ (Alg.1.3)

end for

At the i th layer, Momentum-Net performs the following three processes:

- *Refining:* The i th image refining module gives the “refined” image $z^{(i+1)}$, by applying the i th refining NN, $\mathcal{R}_{\theta^{(i+1)}}$, to an input image at the i th layer, $x^{(i)}$ (i.e., reconstructed image at the $(i - 1)$ th layer). Different from existing INNs, e.g., ADMM-Net [20], PnP [40], RED [22], MoDL [30], BCD-Net [25] (see Fig. 1(b)), TNRD [21], [28], we apply ρ -relaxation with $\rho \in (0, 1)$; see (Alg.1.1). We observed that appropriate selection of ρ can improve MBIR accuracy.
- *Extrapolation:* While the i th layer refining module is refining the i th layer input $x^{(i)}$ (see above), the i th extrapolation module gives the extrapolated point $\hat{x}^{(i+1)}$, based on *momentum* terms $x^{(i)} - x^{(i-1)}$; see (Alg.1.2). Intuitively speaking, momentum is information from previous differences to amplify the changes in subsequent layers. Its effectiveness is shown in diverse optimization literature, e.g., convex optimization [44], [45] and block optimization [24], [35].
- *MBIR:* Given a refined image $z^{(i+1)}$ and a measurement

vector y , the i th MBIR module (Alg.1.3) applies the proximal operator $\text{Prox}_{\tilde{M}^{(i+1)}}(\cdot)$ to the *extrapolated gradient update using a quadratic majorizer* of $F(x; y, z^{(i+1)})$, i.e., $\hat{x}^{(i+1)} - (\tilde{M}^{(i+1)})^{-1} \nabla F(\hat{x}^{(i+1)}; y, z^{(i+1)})$, where $F(x; y, z)$ is defined in (P0). Intuitively speaking, it solves a *majorized* version of the following MBIR problem at the extrapolated point $\hat{x}^{(i+1)}$:

$$\min_{x \in \mathcal{X}} F(x; y, z^{(i+1)}), \quad (\text{P1})$$

and gives a reconstructed image $x^{(i+1)}$. In Momentum-Net, we consider (non)convex differentiable MBIR cost functions $F(x; y, z^{(i+1)})$ with M -Lipschitz continuous gradients, and a convex and closed set \mathcal{X} . For a wide range of large-scale inverse imaging problems, the majorized MBIR problem (Alg.1.3) has a practical closed-form solution and thus, does not require an iterative solver, given the assumptions above and practically invertible majorization matrices $M^{(i+1)}$, e.g., scaled identity, diagonal, and circulant matrices. The updated image $x^{(i+1)}$ is the input to the next Momentum-Net layer.

The followings are details of Momentum-Net in Algorithm 1. A scaled majorization matrix is

$$\tilde{M}^{(i+1)} = \lambda \cdot M^{(i+1)} \succ 0, \quad \lambda \geq 1, \quad (7)$$

where $M^{(i+1)} \in \mathbb{R}^{N \times N}$ is a symmetric positive definite majorization matrix of $\nabla F(x; y, z^{(i+1)})$ in the sense of M -Lipschitz continuity (see Definition 1). In (7), $\lambda = 1$ and $\lambda > 1$ for convex and nonconvex $F(x; y, z^{(i+1)})$ (or convex and nonconvex $f(x; y)$), respectively. We design the extrapolation matrices in the following form:

for convex $f(x; y)$,

$$E^{(i+1)} = \delta^2 m^{(i)} \cdot (M^{(i+1)})^{-\frac{1}{2}} (M^{(i)})^{\frac{1}{2}}; \quad (8)$$

for nonconvex $f(x; y)$,

$$E^{(i+1)} = \delta^2 m^{(i)} \cdot \frac{\lambda - 1}{2(\lambda + 1)} \cdot (M^{(i+1)})^{-\frac{1}{2}} (M^{(i)})^{\frac{1}{2}}, \quad (9)$$

for some $\delta < 1$ and $\{0 \leq m^{(i)} \leq 1 : \forall i\}$, to satisfy conditions (13) and (14) below, respectively. We update the momentum coefficients $\{m^{(i+1)} : \forall i\}$ by the following formula [24], [35]:

$$m^{(i+1)} = \frac{\theta^{(i)} - 1}{\theta^{(i+1)}}, \quad \theta^{(i+1)} = \frac{1 + \sqrt{1 + 4(\theta^{(i)})^2}}{2}; \quad (10)$$

if $F(x; y, z^{(i+1)})$ has a sharp majorizer, i.e., $\nabla F(x; y, z^{(i+1)})$ has $M^{(i+1)}$ such that the corresponding bound in Definition 1 is tight, then we set $m^{(i+1)} = 0, \forall i$.

2.3 Relations to previous works

Several existing MBIR methods can be viewed as a special case of Momentum-Net:

Example 3. (MBIR model (1) using convolutional autoencoders that satisfy the TF condition [24]). The BPEG-M updates in (3)–(5) are special cases of the modules in Momentum-Net (Algorithm 1), with $\{\mathcal{R}_{\theta^{(i+1)}}(\cdot) = \sum_{k=1}^K \text{flip}(h_k^*) * \mathcal{T}_{\beta_k}(h_k * (x^{(i)})) : \forall i\}$ (i.e., convolutional autoencoder [24]) and $\rho \approx 1$.

Example 4. (INNs inspired by gradient descent method, e.g., TNRD [21], [28]). Removing extrapolation modules, i.e.,

setting $\{E^{(i+1)} = 0 : \forall i\}$ in (Alg.1.2), and setting $\rho \approx 1$, Momentum-Net becomes the existing INN in [21], [28].

Example 5. (BCD-Net for image denoising [25]). To obtain a clean image $x \in \mathbb{R}^N$ from a noisy image $y \in \mathbb{R}^N$ corrupted by an additive white Gaussian noise (AWGN), MBIR problem (P1) considers the data-fit $f(x; y) = \frac{1}{2} \|y - x\|_W^2$ with the inverse covariance matrix $W = \frac{1}{\sigma^2} I$, where σ^2 is a variance of AWGN, and the box constraint $\mathcal{X} = [0, U]^N$ with an upper bound $U > 0$. For this $f(x; y)$, the MBIR module (Alg.1.3) can use the exact majorizer $\{\tilde{M}^{(i+1)} = (\frac{1}{\sigma^2} + \gamma)I\}$ and one does not need to use the extrapolation module (Alg.1.2), i.e., $\{E^{(i+1)} = 0\}$. Thus, Momentum-Net (with $\rho \approx 1$) becomes BCD-Net.

Example 6. (BCD-Net for undersampled single-coil MRI [25]). To obtain an object magnetization $x \in \mathbb{R}^N$ from a k -space data $y \in \mathbb{C}^m$ obtained by undersampling (e.g., compressed sensing [48]) MRI, MBIR problem (P1) considers the data-fit $f(x; y) = \frac{1}{2} \|y - Ax\|_W^2$ with an undersampling Fourier operator A (disregarding relaxation effects and considering Cartesian k -space), the inverse covariance matrix $W = \frac{1}{\sigma^2} I$, where σ^2 is a variance of complex AWGN [49], and $\mathcal{X} = \mathbb{C}^N$. For this $f(x; y)$, the MBIR module (Alg.1.3) can use the exact majorizer $\{\tilde{M}^{(i+1)} = F_{\text{disc}}^H (\frac{1}{\sigma^2} P + \gamma I) F_{\text{disc}}\}$ that is practically invertible, where F_{disc} is the discrete Fourier transform and P is a diagonal matrix with either 0 or 1 (their positions correspond to sampling pattern in k -space), and the extrapolation module (Alg.1.2) uses the zero extrapolation matrices $\{E^{(i+1)} = 0\}$. Thus, Momentum-Net (with $\rho \approx 1$) becomes BCD-Net.

In constructing INN architectures for MBIR, generalizing the block-wise optimization updates that solve (1) has benefits over existing generalization methods, PnP [23], [38], [40] and RED [22], [42]; see Remark 7 below. Examples include generalizing BPEG-M and BCD algorithms that solve (1) to construct Momentum-Net and BCD-Net [25], respectively.

Remark 7. First, the BPEG-M updates in (3)–(5) give a clear mathematical connection between denoisers, e.g., a convolutional autoencoder in (3), and cost functions, e.g., a convolutional regularizer in (1). The similar relations can be found in constructing the BCD-Net architecture in Fig. 1(b) [25]. Different from the proposed generalization approach, such connections are less clear in RED. Particularly when the denoiser itself is obtained from a prior, the RED prior $x^T(x - \mathcal{D}(x))$ [22] is different from the denoiser prior, where \mathcal{D} is a denoiser. For example, the prior term corresponding to the convolutional autoencoder in (3) is the convolutional regularizer, $\min_{\{\zeta_k\}} r(x, \{\zeta_k\}; \{h_k\})$, in (1); but this differs from the RED prior. Second, the proposed generalization approach leads to INN architectures that are free from tuning additional hyperparameters, e.g., ADMM parameter in PnP-ADMM [38], [40]. Different from block-wise optimization updates that solve (1), e.g., BPEG-M updates (3)–(5) and BCD updates [25], ADMM iterates solving $\min_x f(x; y) + \sum_{k=1}^K \beta_k \|h_k * x\|_1$ consist of different combinations of primal, auxiliary, dual variables, and ADMM parameters; more importantly, those require tricky ADMM parameter tuning that depends on applications. Thus, different from our approach, generalizing ADMM updates leads

to INN architectures that require ADMM parameters tuning, e.g., PnP-ADMM [38], [40].

Finally, the remark below summarizes the benefits of Momentum-Net:

Remark 8. The proposed Momentum-Net has several benefits over existing INNs:

- *Benefits from refining module:* The image refining module (Alg.1.1) can use layer-wise image refining NNs $\{\mathcal{R}_{\theta^{(i+1)}} : i \geq 0\}$: those are particularly useful to regulate overfitting risks by reducing dimensions of their parameters $\theta^{(i+1)}$ at each layer; see §2.2 and [17], [19]. In addition, different from the existing methods mentioned in §1.2, (Alg.1.1) does not require (firmly) nonexpansive mapping operators $\{\mathcal{R}_{\theta^{(i+1)}}\}$ to guarantee convergence of Momentum-Net. Instead, $\{\mathcal{R}_{\theta^{(i+1)}}\}$ in (Alg.1.1) assumes a substantially weaker notion than the (firm) non-expansiveness which is an assumed condition for convergence of the existing methods including PnP [20], [23], [38]–[40], RED [22], [42], etc.; see Definition 9 in the next section.
- *Benefits from extrapolation module:* The extrapolation module (Alg.1.2) uses the momentum terms $x^{(i)} - x^{(i-1)}$, and those are particularly useful to accelerate the convergence of Momentum-Net. In particular, compared to the existing gradient-descent-inspired INNs (i.e., Momentum-Net using no extrapolation modules), e.g., TNRD [21], [28], Momentum-Net converges faster; see Figs. 3–4 later. (Note that the way the authors of [42] used momentum is less conventional. The corresponding method, RED-APG [42, Alg. 6], still can require multiple inner iterations to solve its quadratic MBIR problem, similar to BCD-Net-type methods.)
- *Benefits from MBIR module:* The MBIR module (Alg.1.3) does not require multiple iterations for a wide range of imaging problems and has both theoretical and practical benefits. Note first that convergence analysis of INNs (including Momentum-Net) assumes that their MBIR operators are *noniterative*. In other words, related convergence theory (e.g., Proposition 14) will fall apart if iterative methods, particularly with insufficient number of iterations, are applied to MBIR modules. Different from the existing BCD-Net-type methods [20], [22], [23], [25], [30], [38]–[40], [42] that can require iterative solvers for their MBIR modules, MBIR module (Alg.1.3) of Momentum-Net can have practical close-form solution, and its corresponding convergence analysis (see §2.4) can hold stably for a wide range of imaging applications. Second, combined with extrapolation module (Alg.1.2), noniterative MBIR modules (Alg.1.3) lead to faster MBIR, compared to the existing BCD-Net-type methods that can require multiple iterations for their MBIR modules for convergence; see Figs. 3–4 later. Third, Momentum-Net guarantees convergence even for nonconvex MBIR cost function $F(x; y, z)$ or nonconvex data-fit $f(x; y)$ of which the gradient is M -Lipschitz continuous (see Definition 1), while existing INNs overlooked nonconvex $F(x; y, z)$ or $f(x; y)$. Finally, different from existing gradient-descent-inspired INNs (e.g., TNRD [21], [28]), Momentum-Net does not require sophisticated step-size control or backtracking

schemes.

Furthermore, see the convergence property comparisons between Momentum-Net and BCD-Net in Appendix B. The following section analyzes the convergence of Momentum-Net.

2.4 Convergence analysis

There are two key challenges in analyzing the convergence of Momentum-Net in Algorithm 1: both challenges relate to its image refining modules (Alg.1.1). First, image refining NNs $\mathcal{R}_{\theta^{(i+1)}}$ change across layers; even if they are identical across layers, they are not necessarily nonexpansive operators [50], [51] in practice. Second, the layer-wise refining NNs $\{\mathcal{R}_{\theta^{(i+1)}} : \forall i\}$ are not necessarily proximal mapping operators, i.e., they are not written explicitly in the form of (2) (or no explicit corresponding cost function exists). This section proposes two new asymptotic definitions to overcome the aforementioned challenges, and then uses those conditions to analyze convergence properties of Momentum-Net in Algorithm 1.

2.4.1 Preliminaries

To resolve the challenge of layer-wise refining NNs $\{\mathcal{R}_{\theta^{(i+1)}} : \forall i\}$ and the practical difficulty in guaranteeing their non-expansiveness, we introduce the following generalized definition of the non-expansiveness [50], [51].

Definition 9 (Asymptotically nonexpansive paired operators). A sequence of paired operators $(\mathcal{R}_{\theta^{(i)}}, \mathcal{R}_{\theta^{(i+1)}})$ is *asymptotically nonexpansive* if there exist a summable nonnegative sequence $\{\epsilon^{(i+1)} \geq 0 : \sum_{i=0}^{\infty} \epsilon^{(i+1)} < \infty\}$ such that²

$$\|\mathcal{R}_{\theta^{(i+1)}}(u) - \mathcal{R}_{\theta^{(i)}}(v)\|_2^2 \leq \|u - v\|_2^2 + \epsilon^{(i+1)}, \quad \forall u, v, i. \quad (11)$$

Observe that when $\mathcal{R}_{\theta^{(i+1)}} = \mathcal{R}_{\theta}$ and $\epsilon^{(i+1)} = 0$, $\forall i$, Definition 9 becomes the standard non-expansiveness of an mapping operator \mathcal{R}_{θ} . If we replace the inequality (\leq) with the strict inequality ($<$) in (11), then we say that the sequence of paired operators $(\mathcal{R}_{\theta^{(i+1)}}, \mathcal{R}_{\theta^{(i)}})$ is asymptotically contractive. (This stronger assumption is used to prove convergence of BCD-Net [25] in Proposition 14.) Definition 9 also implies that mapping operators $\mathcal{R}_{\theta^{(i+1)}}$ converge to some nonexpansive operator, if the corresponding parameters $\theta^{(i+1)}$ converge.

Definition 9 incorporates the pairing property into the standard non-expansiveness of operators, since Momentum-Net uses layer-wise image refining NNs. Specifically, the pairing property is useful for proving convergence of Momentum-Net, by connecting image refining NNs at the current layer and the previous layer, i.e., $\mathcal{R}_{\theta^{(i+1)}}$ and $\mathcal{R}_{\theta^{(i)}}$, respectively. Furthermore, the asymptotic property in Definition 9 allows Momentum-Net to use *expansive* refining NNs (i.e., mapping operators having a Lipschitz constant larger than 1) for some layers, while guaranteeing convergence; see Figs. 2(a3) and (b3) below. Suppose that refining NNs are identical across layers, i.e., $\mathcal{R}_{\theta^{(i+1)}} = \mathcal{R}_{\theta}$, $\forall i$, similar to some existing INNs, e.g., PnP [23], RED [22], and

2. One could replace the bound in (11) with $\|\mathcal{R}_{\theta^{(i+1)}}(u) - \mathcal{R}_{\theta^{(i)}}(v)\|_2^2 \leq (1 + \epsilon^{(i+1)})\|u - v\|_2^2$ (and summable $\{\epsilon^{(i+1)} : \forall i\}$), and the proofs for our main arguments go through.

other methods in §1.2. In such cases, if \mathcal{R}_θ is expansive, Momentum-Net may diverge; this property corresponds to the limitation of existing methods described in §1.2. Momentum-Net moderates this issue by using layer-wise refining NNs that satisfy the asymptotic non-expansiveness in Definition 9.

Because the sequence $\{z^{(i+1)} : \forall i\}$ in (Alg.1.1) is not necessarily updated with a proximal mapping $\{\mathcal{R}_{\theta(i+1)} : \forall i\}$ (and $\rho \approx 1$), we introduce a generalized definition of block-coordinate minimizers [52, (2.3)] for $z^{(i+1)}$ -updates:

Definition 10 (Asymptotic block-coordinate minimizer). *The update $z^{(i+1)}$ is an asymptotic block-coordinate minimizer if there exists a summable nonnegative sequence $\{\Delta^{(i+1)} \geq 0 : \sum_{i=0}^{\infty} \Delta^{(i+1)} < \infty\}$ such that*

$$\|x^{(i)} - z^{(i+1)}\|_2^2 \leq \|x^{(i)} - z^{(i)}\|_2^2 + \Delta^{(i+1)}, \quad \forall i. \quad (12)$$

Definition 10 implies that as $i \rightarrow \infty$, the updates $\{z^{(i+1)} : i \geq 0\}$ approach a block-coordinate minimizer trajectory that satisfies (12) with $\{\Delta^{(i+1)} = 0 : i \geq 0\}$. In particular, $\Delta^{(i+1)}$ quantifies how much the update $z^{(i+1)}$ in (Alg.1.1) perturbs a block-coordinate minimizer trajectory. The bound $\|z^{(i+1)} - x^{(i)}\|_2^2 \leq \|z^{(i)} - x^{(i)}\|_2^2$ always holds, $\forall i$, when one uses the proximal mapping in (3) within the BPEG-M framework.

2.4.2 Assumptions

This section introduces and interprets the assumptions for convergence analysis of Momentum-Net in Algorithm 1:

- *Assumption 1*) In MBIR problems (P1), (non)convex $F(x; y, z^{(i+1)})$ is (continuously) differentiable, proper, and lower-bounded in $\text{dom}(F)$,³ and \mathcal{X} is convex and closed, $\forall i$. For any given nonexpansive refiner \mathcal{R}_θ and symmetric positive definite majorization matrix M , Algorithm 1 has a fixed-point.
- *Assumption 2*) $\nabla F(x; y, z^{(i+1)})$ is $M^{(i+1)}$ -Lipschitz continuous with respect to x , specifically,

$$\begin{aligned} & \left\| \nabla F(u; y, z^{(i+1)}) - \nabla F(v; y, z^{(i+1)}) \right\|_{(M^{(i+1)})^{-1}} \\ & \leq \|u - v\|_{M^{(i+1)}}, \end{aligned}$$

$\forall u, v \in \mathbb{R}^N$, where $M^{(i+1)}$ is a layer-wise majorization matrix that satisfies $m_{F,\min} I_N \preceq M^{(i+1)} \preceq m_{F,\max} I_N$ with $0 < m_{F,\min} \leq m_{F,\max} < \infty$, $\forall i$.

- *Assumption 3*) The extrapolation matrices $E^{(i+1)} \succeq 0$ in (8)–(9) satisfy the following conditions:

for convex $f(x; y)$,

$$(E^{(i+1)})^T M^{(i+1)} E^{(i+1)} \preceq \delta^2 \cdot M^{(i)}, \quad \delta < 1; \quad (13)$$

for nonconvex $f(x; y)$,

$$(E^{(i+1)})^T M^{(i+1)} E^{(i+1)} \preceq \frac{\delta^2(\lambda - 1)^2}{4(\lambda + 1)^2} \cdot M^{(i)}, \quad \delta < 1. \quad (14)$$

- *Assumption 4*) The sequence of paired operators $(\mathcal{R}_{\theta(i+1)}, \mathcal{R}_{\theta(i)})$ is asymptotically nonexpansive with a summable sequence $\{\epsilon^{(i+1)} \geq 0\}$; the update $z^{(i+1)}$ is an asymptotic block-coordinate minimizer with a

summable sequence $\{\Delta^{(i+1)} \geq 0\}$. The mapping functions $\{\mathcal{R}_{\theta(i+1)} : \forall i\}$ are continuous and the corresponding parameters $\{\theta^{(i+1)} : \forall i\}$ are bounded.

Assumption 1 is a slight modification of Assumption S.1 of BPEG-M, and Assumptions 2–3 are identical to Assumptions S.2–S.3 of BPEG-M; see Assumptions S.1–S.3 in §S.1.3.

Below we provide empirical justifications for the first two conditions in Assumption 4. First, Fig. 2(a2) illustrates that paired refining NNs $(\mathcal{R}_{\theta(i+1)}, \mathcal{R}_{\theta(i)})$ of Momentum-Net appear to be asymptotically nonexpansive in an application that has mild data-fit variations across training samples. We also observed for different applications that refining NNs $\{\mathcal{R}_{\theta(i+1)}\}$ become nonexpansive: those at the first several layers can be expansive, and those in later layers become nonexpansive. See Figs. 2(a3) and 2(b3).

Second, we observed for different applications that the $z^{(i+1)}$ -updates are asymptotic block-coordinate minimizers; see Figs. 2(a1) and 2(b1). Lemma S.4 and §S.2 in the supplement provide a *probabilistic* justification for the asymptotic block-coordinate minimizer condition.

Finally, we remark that Example 3 above satisfies the two asymptotic conditions in Assumption 4. In particular, the convolutional autoencoder in (3) that satisfies the TF condition in §2.1 is nonexpansive [27]; update (3) leads to a block coordinate minimizer $z^{(i+1)}$ because the convolutional autoencoder in (3) is a proximal mapping operator.

2.4.3 Main convergence results

This section analyzes fixed-point and critical point convergence of Momentum-Net in Algorithm 1, under the assumptions in the previous section. We first show that differences between two consecutive iterates generated by Momentum-Net converge to zero:

Proposition 11 (Convergence properties). *Under Assumptions 1–4, let $\{x^{(i+1)}, z^{(i+1)} : i \geq 0\}$ be the sequence generated by Algorithm 1. Then, the sequence satisfies*

$$\sum_{i=0}^{\infty} \left\| \begin{bmatrix} x^{(i+1)} \\ z^{(i+1)} \end{bmatrix} - \begin{bmatrix} x^{(i)} \\ z^{(i)} \end{bmatrix} \right\|_2^2 < \infty, \quad (15)$$

and hence $\left\| \begin{bmatrix} x^{(i+1)} \\ z^{(i+1)} \end{bmatrix} - \begin{bmatrix} x^{(i)} \\ z^{(i)} \end{bmatrix} \right\|_2 \rightarrow 0$.

Proof. See §S.3 of the supplementary material.

Using Proposition 11, our main theorem provides that any limit points of the sequence generated by Momentum-Net converges to a point that satisfies critical point and fixed-point conditions:

Theorem 12 (A limit point satisfies both critical point and fixed-point conditions). *Under Assumptions 1–4 above, let $\{x^{(i+1)}, z^{(i+1)} : i \geq 0\}$ be the sequence generated by Algorithm 1. Consider either a fixed majorization matrix with general structures, i.e., $M^{(i+1)} = M$ for $i \geq 0$, or a sequence of diagonal majorization matrices, i.e., $\{M^{(i+1)} : i \geq 0\}$. Then, any limit point \bar{x} of $\{x^{(i+1)}\}$ satisfies both the critical point condition:*

$$\langle \nabla F(\bar{x}; y, \bar{z}), x - \bar{x} \rangle \geq 0, \quad \forall x \in \mathcal{X}, \quad (16)$$

where \bar{z} is a limit point of $\{z^{(i+1)}\}$, and the fixed-point condition:

$$\begin{bmatrix} \bar{x} \\ \bar{x} \end{bmatrix} = \mathcal{A}_{\mathcal{R}_\theta}^M \left(\begin{bmatrix} \bar{x} \\ \bar{x} \end{bmatrix} \right), \quad (17)$$

3. $F : \mathbb{R}^n \rightarrow (-\infty, +\infty]$ is proper if $\text{dom} F \neq \emptyset$. F is lower bounded in $\text{dom}(F) := \{u : F(u) < \infty\}$ if $\inf_{u \in \text{dom}(F)} F(u) > -\infty$.

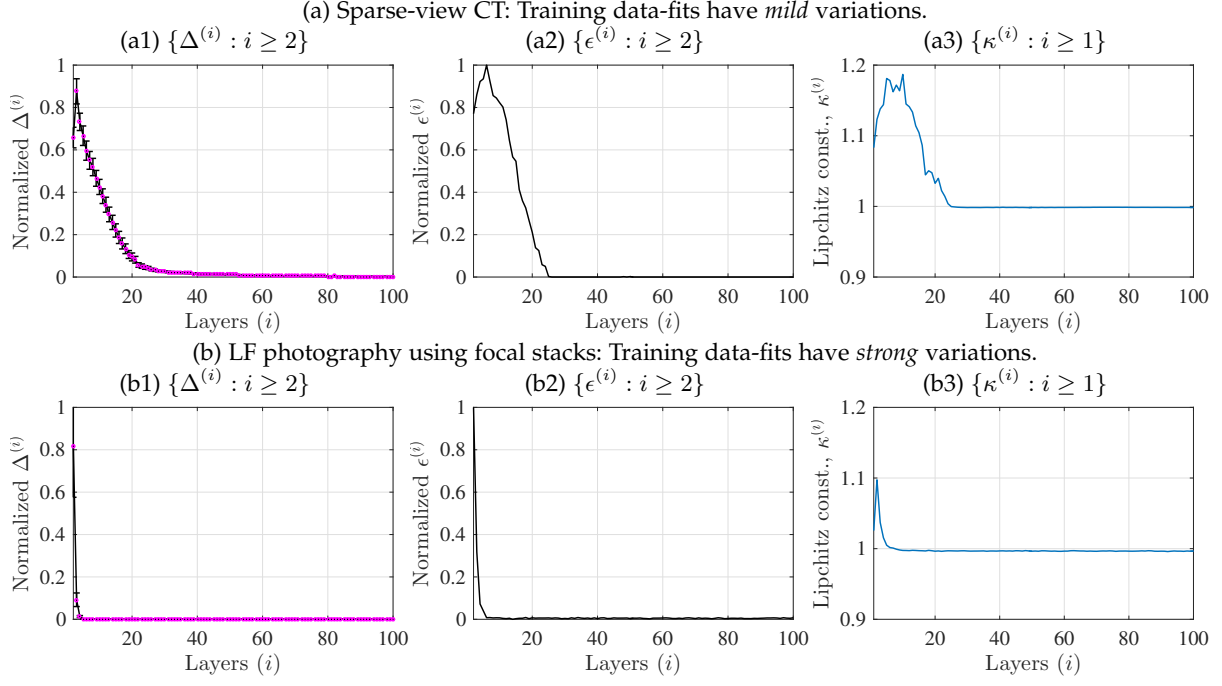


Fig. 2. Empirical measures related to Assumption 4 for guaranteeing convergence of Momentum-Net in different applications (we estimated the sequence $\{\epsilon^{(i)} : i = 2, \dots, N_{\text{Irr}}\}$ in Definition 9, the sequence $\{\Delta^{(i)} : i = 2, \dots, N_{\text{Irr}}\}$ in Definition 10, and the Lipschitz constants $\{\kappa^{(i)} : i = 1, \dots, N_{\text{Irr}}\}$ of refining NNs $\{\mathcal{R}_{\theta^{(i)}} : \forall i\}$, based on a hundred sets of randomly selected training samples related with the corresponding bounds of the measures, e.g., u and v in (11) are training input to $\mathcal{R}_{\theta^{(i+1)}}$ and $\mathcal{R}_{\theta^{(i)}}$ in (Alg.1.1), respectively). (a) The sparse-view CT reconstruction experiment used fan-beam geometry with 12.5% projections views. (b) The LF photography experiment used five detectors and reconstructed LFs consisting of 9×9 sub-aperture images. (a1, b1) For both the applications, we observed that $\Delta^{(i)} \rightarrow 0$. This implies that the $z^{(i+1)}$ -updates in (Alg.1.1) satisfy the asymptotic block-coordinate minimizer condition in Assumption 4. (a2) Momentum-Net trained from training samples with *mild* variations in data-fits show that $\epsilon^{(i)} \rightarrow 0$. This implies that paired NNs $(\mathcal{R}_{\theta^{(i+1)}}, \mathcal{R}_{\theta^{(i)}})$ in (Alg.1.1) are asymptotically nonexpansive. (b2) Momentum-Net trained from training samples with *strong* variations in data-fits show that $\epsilon^{(i)}$ becomes close to zero, but does not converge to zero. (a3, b3) The NNs, $\mathcal{R}_{\theta^{(i+1)}}$ in (Alg.1.1), become nonexpansive, i.e., its Lipschitz constant $\kappa^{(i)}$ becomes smaller than 1, as i increases.

where $\begin{bmatrix} x^{(i+1)} \\ x^{(i)} \end{bmatrix} = \mathcal{A}_{\mathcal{R}_{\theta^{(i+1)}}}^{M^{(i+1)}} \left(\begin{bmatrix} x^{(i)} \\ x^{(i-1)} \end{bmatrix} \right)$, $\mathcal{A}_{\mathcal{R}_{\theta^{(i+1)}}}^{M^{(i+1)}}(\cdot)$ denotes performing the i th updates in Algorithm 1, and θ and \bar{M} is a limit point of $\{\theta^{(i+1)}\}$ and $\{M^{(i+1)}\}$, respectively.

Proof. See §S.4 of the supplementary material.

Observe that, if $\mathcal{X} = \mathbb{R}^N$ or \bar{x} is an interior point of \mathcal{X} , (16) reduces to the first-order optimality condition $0 \in \partial F(\bar{x}; y, \bar{z})$, where $\partial F(x)$ denotes the limiting subdifferential of F at x . With additional isolation and boundedness assumptions for the points satisfying (16) and (17), we obtain whole sequence guarantees:

Corollary 13 (Whole sequence convergence). *Consider the construction in Theorem 12. Let \mathcal{S} be the set of points satisfying the critical point condition in (16) and the fixed-point condition in (17). If $\{x^{(i+1)} : i \geq 0\}$ is bounded, we obtain $\text{dist}(x^{(i+1)}, \mathcal{S}) \rightarrow 0$, where $\text{dist}(u, \mathcal{V}) := \inf\{\|u - v\| : v \in \mathcal{V}\}$ denotes the distance from u to \mathcal{V} , for any point $u \in \mathbb{R}^N$ and any subset $\mathcal{V} \subset \mathbb{R}^N$. If \mathcal{S} contains uniformly isolated points, i.e., there exists $\eta > 0$ such that $\|u - v\| \geq \eta$ for any distinct points $u, v \in \mathcal{S}$, then $\{x^{(i+1)}\}$ converges to a point in \mathcal{S} .*

Proof. See §S.5 of the supplementary material.

The boundedness assumption for $\{x^{(i+1)}\}$ in Corollary 13 is standard in block-wise optimization, e.g., [24], [35], [52]–[54]. The assumption can be satisfied if the set \mathcal{X} is bounded (e.g., box constraints), one chooses appropriate regularization parameters in Algorithm 1 [24], [35], [54], the function $F(x; y, z)$ is coercive [53], or the level set is

bounded [52]. However, for general $F(x; y, z)$, it is hard to verify the isolation condition for the points in \mathcal{S} in practice. Instead, one may use Kurdyka-Łojasiewicz property [52], [53] to analyze the whole sequence convergence with some appropriate modifications.

3 TRAINING INNS

This section describes training of all the INNs compared in this paper, including BCD-Net [25] (i.e., general case of RED [22] and MoDL [30]), Momentum-Net without extrapolation (i.e., general case of TNRD [21], [28]), and the proposed Momentum-Net that uses extrapolation.

3.1 Architecture of refining NNs and their training

For all INNs in this paper, we train the refining NN $\mathcal{R}_{\theta^{(i+1)}}$ at each layer, to remove some artifacts on the input image $x^{(i)}$ that is fed from the previous layer. For the i th layer NN, we consider the following residual [55] convolutional autoencoder architecture:

$$\mathcal{R}_{\theta^{(i+1)}}(u) = \sum_{k=1}^K d_k^{(i+1)} * \mathcal{T}_{\exp(\alpha_k^{(i+1)})}(e_k^{(i+1)} * u) + u, \quad (18)$$

where $\theta^{(i+1)} = \{d_k^{(i+1)}, \alpha_k^{(i+1)}, e_k^{(i+1)} : \forall k\}$ is the parameter set of the i th image refining NN, $\{d_k^{(i+1)}, e_k^{(i+1)} \in \mathbb{C}^R : k = 1, \dots, K\}$ is a set of K decoding and encoding filters of size R , $\{\exp(\alpha_k^{(i+1)}) : k = 1, \dots, K\}$ is a set of K thresholding values, and $\mathcal{T}_\alpha(u)$ is the soft-thresholding operator with

parameter α defined in (6), for $i = 0, \dots, N_{\text{lyr}} - 1$. In particular, we include the exponential function $\exp(\cdot)$ to prevent the thresholding parameters $\{\alpha_k\}$ from becoming zero during training. We observed that the residual convolutional autoencoder in (18) gives better results compared to the convolutional autoencoder, i.e., (18) without the second term [19], [25]. This corresponds to the empirical result in [56] that having skip connections [55] (e.g., the second term in (18)) produced more benign optimization landscapes in training, and well-chosen training parameters gave optimizer that generalize better. (In addition, we observed that having the skip connection in (18) eases tuning learning rates.)

The training process of Momentum-Net requires L high-quality training images (e.g., ground truths), $\{x_l : l = 1, \dots, L\}$, L training measurements simulated via imaging physics, $\{y_l : l = 1, \dots, L\}$, and L data-fits $\{f_l(x; y_l) : l = 1, \dots, L\}$ and the corresponding majorization matrices $\{M_l^{(i)}, \widetilde{M}_l^{(i)} : l = 1, \dots, L, i = 1, \dots, N_{\text{lyr}}\}$. Different from [17], [25] that trains convolutional autoencoders from the patch perspective, we train the image refining NNs in (18) from the convolution perspective (that does not store many overlapping patches, e.g., see [24]). From L training pairs $(x_l, x_l^{(i)})$, where $\{x_l^{(i)} : l = 1, \dots, L\}$ is a set of L reconstructed images at the $(i - 1)$ th Momentum-Net layer, we train the i th layer image refining NN in (18) by solving the following optimization problem:

$$\theta^{(i+1)} = \underset{\theta}{\operatorname{argmin}} \frac{1}{2L} \sum_{l=1}^L \|x_l - \mathcal{R}_\theta(x_l^{(i)})\|_2^2, \quad (\text{P2})$$

where $\theta^{(i+1)}$ is given as in (18), for $i = 0, \dots, N_{\text{lyr}} - 1$. The convolutional training loss in (P2) has three advantages over the patch-based training loss in [17], [25] that may use all the extracted overlapping patches of size R (see details in §S.6.1 with Lemma S.5):

- The corresponding patch-based loss does not model the patch aggregation process that is inherently modeled in (18).
- It is an upper bound of the convolutional loss (P2).
- It requires about R times more memory than (P2).

We solve the training optimization problems (P2) by mini-batch stochastic optimization with the subdifferentials given in §S.7.

3.2 Regularization parameter selection based on condition numbers

When training data-fits $\{f_l(x; y_l) : l = 1, \dots, L\}$ are reasonably similar, the regularization parameter γ in (P1) is trainable by substituting (Alg.1.1) into (Alg.1.3) and modifying the training cost (P2). However, training data-fits can greatly differ due to various reasons, including a wide variety of imaging geometries or image formation systems, and noise levels in training measurements $\{y_l\}$, constructing datasets with sufficient size by including various $\{f_l(x; y_l)\}$, etc. See such examples in §4.1–4.2.

To train Momentum-Net with different training data-fits, we propose a parameter selection scheme based on the spectral radius of their majorization matrices $\{M_{f_l}^{(i)}\}$. For simplicity, consider that majorization matrices of training

MBIR problems (P1) are given by $\widetilde{M}_l^{(i)} = \widetilde{M}_l = \lambda(M_{f_l} + \gamma I)$, where the majorization scaling factor λ is selected by (7) and M_{f_l} is a symmetric positive semidefinite majorization matrix for $f_l(x; y_l)$, $\forall i, l$. We select the regularization parameter γ_l for the l th training sample as

$$\gamma_l = \frac{r(M_{f_l})}{\chi^*}, \quad (\text{19})$$

where the spectral radius of a matrix is defined by $r(\cdot) := \sigma_{\max}(\cdot) - \sigma_{\min}(\cdot)$ for $\sigma_{\max}(M_{f_l}) > \sigma_{\min}(M_{f_l}) \geq 0$, and $\sigma_{\max}(\cdot)$ and $\sigma_{\min}(\cdot)$ are the largest and smallest eigenvalues of a matrix, respectively. For the l th training sample, a desired factor χ^* controls γ_l in (19) according to $r(M_{f_l})$, $\forall l$. The proposed parameter selection scheme also applies to testing Momentum-Net, based on the identical desired factor χ^* used in its training. We observed that the proposed parameter selection scheme gives better MBIR accuracy compared to the condition number based selection scheme that is similarly used in selecting ADMM parameters [18] (for the two applications in §4). One may further apply this scheme to layer-wise majorization matrices $\widetilde{M}_l^{(i)}$ and select layer-wise regularization parameters $\gamma_l^{(i)}$ accordingly.

4 EXPERIMENTAL RESULTS AND DISCUSSION

We investigated two extreme imaging applications: sparse-view CT and LF photography using a focal stack. In particular, these two applications do not have practical closed-form solution for MBIR modules of BCD-Net, i.e., solving (Alg.2.2). For these applications, we compared the performances of the following three INNs: BCD-Net [25] (i.e., general case of RED [22] and MoDL [30]), Momentum-Net *without extrapolation* (i.e., general case of TNRD [21], [28]), and the proposed Momentum-Net using extrapolation.

4.1 Experimental setup: Imaging

4.1.1 Sparse-view CT

To reconstruct a linear attenuation coefficient image $x \in \mathbb{R}^N$ from post-log sinogram $y \in \mathbb{R}^m$ in sparse-view CT, the MBIR problem (P1) considers a data-fit $f(x; y) = \frac{1}{2} \|y - Ax\|_W^2$ and the non-negativity constraint $\mathcal{X} = [0, \infty]^N$, where $A \in \mathbb{R}^{m \times N}$ is an undersampled CT system matrix, $W \in \mathbb{R}^{m \times m}$ is a diagonal weighting matrix with elements $\{W_{w,w} = p_w^2 / (p_w + \sigma^2) : \forall w\}$ based on a Poisson-Gaussian model [18], [57] for the pre-log raw measurements $p \in \mathbb{R}^m$ with electronic readout noise variance σ^2 .

We simulated 2D sparse-view sinograms of size $m = 888 \times 123$ – ‘detectors or rays’ \times ‘regularly spaced projection views or angles’, where 984 is the number of full views – with GE LightSpeed fan-beam geometry corresponding to a monoenergetic source with 10^5 incident photons per ray and no background events, and electronic noise variance $\sigma^2 = 5^2$. We avoided an inverse crime in imaging simulation and reconstructed images of size $N = 420 \times 420$ with a coarser grid $\Delta_x = \Delta_y = 0.9766$ mm; see details in [37, §V-A2].

4.1.2 LF photography using a focal stack

To reconstruct a LF $x = [x_1^T, \dots, x_S^T]^T \in \mathbb{R}^{SN'}$ that consists of S sub-aperture images from focal stack measurements $y = [y_1^T, \dots, y_C^T]^T \in \mathbb{R}^{CN'}$ that are collected by C

photosensors, the MBIR problem (P1) considers a data-fit $f(x; y) = \frac{1}{2}\|y - Ax\|_2^2$ and a box constraint $\mathcal{X} = [0, U]^{SN'}$ with $U=1$ (or 255 without rescaling), where $A \in \mathbb{R}^{CN' \times SN'}$ is a system matrix of LF imaging system using focal stacks that is constructed blockwise with $C \cdot S$ different convolution matrices $\{\tau_c A'_{c,s} \in \mathbb{R}^{N' \times N'} : c=1, \dots, C, s=1, \dots, S\}$ [47], $\tau_c \in (0, 1]$ is a transparency coefficient for the c th detector,⁴ and N' is the size of sub-aperture images, $x_s, \forall s$. In general, LF photography system using focal stacks has extremely ill-conditioned A , because $C \ll S$.

To avoid an inverse crime, our imaging simulation used higher-resolution synthetic LF dataset [59] (we converted the original RGB sub-aperture to grayscale sub-aperture images by the “rgb2gray.m” function in MATLAB, for simplicity and smaller memory requirements in training). We simulated $C=5$ focal stack images of size $N'=255 \times 255$ with 40 dB AWGN that models electronic noise at sensors, and setting transparency coefficients τ_c as 1, for $c=1, \dots, C$. The sensor positions were chosen such that five sensors focus at equally spaced depths; specifically, the closest sensor to scenes and farthest sensor from scenes focus at two different depths that correspond to ‘disp_{min} + 0.2’ and ‘disp_{max} - 0.2’, respectively, where disp_{max} and disp_{min} are the approximate maximum and minimum disparity values specified in [59]. We reconstructed 4D LFs that consist of $S=9 \times 9$ sub-aperture images of size $N'=255 \times 255$, with a coarser grid $\Delta_x = \Delta_y = 0.13572$ mm.

4.2 Experimental setup: INNs

4.2.1 Parameters of INNs

The parameters for the INNs compared in sparse-view CT experiments were defined as follows. We considered two BCD-Nets: for one BCD-Net, we applied the APG method [45] with 10 iterations to (Alg.2.2), and set $N_{\text{lyr}} = 30$; for the other BCD-Net, we applied the APG method with three iterations to (Alg.2.2), and set $N_{\text{lyr}} = 45$. For Momentum-Net without extrapolation, we chose $N_{\text{lyr}} = 100$ and $\rho = 1 - \varepsilon$. For the proposed Momentum-Net, we chose $N_{\text{lyr}} = 100$ and $\rho = 0.5$. For performance comparisons between different INNs, all the INNs used residual convolutional autoencoders (18) with $\{R, K = 7^2\}$. For comparing different MBIR methods, Momentum used extrapolation, i.e., (Alg.1.2) with (8) and (10), and $\{R=7^2, K=9^2\}$ for (18). We designed the majorization matrices as $\{\tilde{M}^{(i+1)} = \text{diag}(A^T W A) + \gamma I : i \geq 0\}$, using Lemma S.6 (note that A and W have nonnegative entries) and setting $\lambda = 1$ by (7). The regularization parameters were selected by the spectral radius based selection scheme in §3.2 with the desired factor $\chi^* = 167.64$.⁵

The parameters for the INNs compared in experiments of LF photography using focal stacks were defined as follows. We considered two BCD-Nets with the identical parameters listed above. For Momentum-Net without

extrapolation and the proposed Momentum-Net, we set $N_{\text{lyr}} = 100$ and $\rho = 1 - \varepsilon$. All the INNs used residual convolutional autoencoders (18) with $\{R = 5^2, K = 32\}$ in the epipolar domain. To generate $\mathcal{R}_{\theta(i+1)}(x^{(i)})$ at the i th refining module of INNs, we applied a single residual NN (18) with $\{R = 5^2, K = 32\}$ to two sets of horizontal and vertical epipolar plane images, and took the average of two LFs that were permuted back from refined horizontal and vertical epipolar plane image sets, $\forall i$.⁶ For comparing different MBIR methods, Momentum-Net used extrapolation and $\{R = 5^2, K = 32\}$ for the epipolar-domain denoiser (18) at each layer. We designed the majorization matrices as $\{\tilde{M}^{(i+1)} = \text{diag}(A^T A) + \gamma I : i \geq 0\}$, using Lemma S.6 (note that A has nonnegative entries) and setting $\lambda = 1$ by (7). The regularization parameters were selected by the proposed selection scheme in §3.2 with the desired factor $\chi^* = 1.5$.⁷

4.2.2 Training INNs

For sparse-view CT experiments, we trained all the INNs from the chest CT dataset with $\{x_l, y_l, f_l(x; y_l) = \frac{1}{2}\|y_l - Ax\|_{W_l}^2, \tilde{M}_l : l = 1, \dots, L, L = 142\}$; we constructed the dataset by using XCAT phantom slices [60] (that is widely used in learning regularizers in an unsupervised manner [18], [24]). For experiments of LF photography using focal stacks, we trained all the INNs from the LF photography dataset with $\{y_l, f_l(x; y_l) = \frac{1}{2}\|y_l - A_l x\|_2^2, \tilde{M}_l : l = 1, \dots, L, L = 21\}$ and two sets of ground truth epipolar images, $\{x_{l,\text{epi-h}}, x_{l,\text{epi-v}} : l = 1, \dots, L, L = 21 \cdot (255 \cdot 9)\}$; we constructed the dataset by excluding four unrealistic “stratified” scenes from the original LF dataset in [59] (that consists of 28 LFs with diverse scene parameter and camera settings).

In training INNs for both the applications, if not specified, we used identical training setups. At each INN layer, we solved (P2) with the mini-batch version of Adam [61] and trained layer-wise residual convolutional autoencoders (18). We selected the batch size and the number of epochs as follows: for sparse-view CT reconstruction, we chose them as 20 and 300; for LF photography using focal stacks, we chose them as 200 and 200. We chose the learning rates for encoding filters $\{e_k^{(i+1)} : \forall k\}$, decoding filters $\{d_k^{(i+1)} : \forall k\}$, and thresholding values $\{\alpha_k^{(i+1)} : \forall k\}$ as 10^{-3} , 10^{-3} , and 10^{-1} , respectively; we reduced the learning rates by 10% every 10 epochs. At the first INN layer, we initialized filter coefficients with Kaiming uniform initialization [62]; in the later INN layers, i.e., at the i th INN layer, for $i \geq 2$, we initialized filter coefficients from those learned from the previous layer, i.e., $(i-1)$ th layer (this also applies to initializing thresholding values).

4.2.3 Testing trained INNs

In sparse-view CT reconstruction experiments, we tested trained INNs to two samples of which ground truth images and the corresponding inverse covariance matrices

4. Traditionally, one obtains focal stacks by physically moving imaging sensors and taking separate exposures across time. Transparent photodetector arrays [58] allows one to collect focal stack data in a single exposure, making a practical LF camera using a focal stack. If some photodetectors are not perfectly transparent, one can use $\tau_c < 1$, for some c .

5. This factor was estimated from the carefully chosen regularization parameter for sparse-view CT MBIR experiments using learned convolutional regularizers in [24].

6. Epipolar images are 2D slices of a 4D LF $L_F(c_x, c_y, c_u, c_v)$, where (c_x, c_y) and (c_u, c_v) are spatial and angular coordinates, respectively. Specifically, each horizontal epipolar plane image are obtained by fixing c_y and c_v , and varying c_x and c_u ; and each vertical epipolar image are obtained by fixing c_x and c_u , and varying c_y and c_v .

7. This factor was selected by considering that the LF photography system is extremely ill-conditioned; see §4.1.2.

(i.e., W in §4.1.1) are sufficiently different from those in training samples (i.e., they are a few cm away from training images). We evaluated the reconstruction quality by the most conventional error metric in CT application, RMSE (in HU), in a region of interest (ROI), where RMSE and HU stand for root-mean-square error and (modified) Hounsfield unit, respectively, and the ROI was a circular region that includes all the phantom tissues. The RMSE is defined by $\text{RMSE}(x^*, x^{\text{true}}) := (\sum_{j=1}^{N_{\text{ROI}}} (x_j^* - x_j^{\text{true}})^2 / N_{\text{ROI}})^{1/2}$, where x^* is a reconstructed image, x^{true} is a ground truth image, and N_{ROI} is the number of pixels in a ROI. In addition, we compared the trained Momentum-Net (using extrapolation) to MBIR method using a conventional hand-crafted EP regularizer, and MBIR model using a learned convolutional regularizer [24], [37] which is the state-of-the-art MBIR method within an unsupervised learning setup. We finely tuned their regularization parameters to achieve the lowest RMSE. See details of these two MBIR models in §S.8.2.

In experiments of LF photography using focal stacks, we tested trained INNs to three samples of which scene parameter and camera settings are different from those in training samples (all training and testing samples have different camera and scene parameters). We evaluated the reconstruction quality by the most conventional error metric in LF photography application, PSNR (in dB), where PSNR stands for peak signal-to-noise. In addition, we compared the trained Momentum-Net (using extrapolation) to MBIR method using the state-of-the-art non-trained regularizer, 4D EP introduced in [47]. (The low-rank plus sparse tensor decomposition model [47], [63] failed when inverse crimes and measurement noise are considered.) We finely tuned its regularization parameter to achieve the lowest RMSE values. See details of this MBIR model in §S.8.3. We further investigated impacts of the LF MBIR quality on a higher-level depth estimation application, by applying the robust Spinning Parallelogram Operator (SPO) depth estimation method [64] to reconstructed LFs.

The imaging simulation and reconstruction experiments were based on the Michigan image reconstruction toolbox [65], and training INNs was based on PyTorch (ver. 0.3.1).

4.3 Comparisons between different INNs

For sparse-view CT and LF photography using a focal stack, the proposed Momentum-Net using extrapolation (significantly) improves MBIR speed and accuracy within a finite time, compared to the existing (soft-refiner) INNs [21]–[23], [25], [28], [30] that correspond to BCD-Net [25] or Momentum-Net using *no extrapolation*. To reach the 26 HU RMSE value in sparse-view CT reconstruction, the proposed Momentum-Net decreases MBIR time by 47.7% and 61.6%, compared to Momentum-Net without extrapolation and BCD-Net using three inner iterations, respectively. To reach the 32 dB PSNR value in LF reconstruction from a focal stack, the proposed Momentum-Net decreases MBIR time by 31.6% and 53.6%, compared to Momentum-Net without extrapolation and BCD-Net using three inner iterations, respectively. See Figs. 3–4. In addition, using extrapolation, i.e., (Alg.1.2) with (8)–(10), improves the performance of Momentum-Net within a finite time; in Figs. 3–4, compare

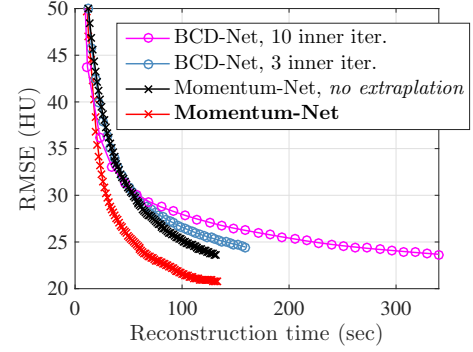


Fig. 3. RMSE minimization comparisons between different INNs for sparse-view CT (fan-beam geometry with 12.5% projections views and 10^5 incident photons; averaged RMSE values across two test samples; single-precision MATLAB implementations were tested on 2.6 GHz Intel Core i7 CPU with 16 GB RAM).

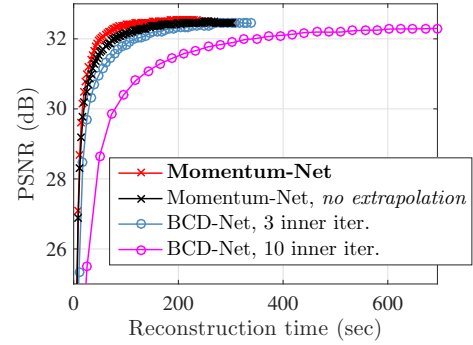


Fig. 4. PSNR maximization comparisons between different INNs in LF photography using a focal stack (LF photography systems with $C = 5$ detectors obtain a focal stack of LFs consisting of $S = 81$ sub-aperture images; averaged PSNR values across three test samples; single-precision MATLAB & PyTorch implementations were tested on 3.5 GHz AMD Threadripper 1920X CPU with 32 GB RAM, and 1531 MHz Nvidia GTX 1080 Ti GPU with 11 GB RAM, respectively).

RMSE and PSNR convergence behaviors of the proposed Momentum-Net and Momentum-Net using no extrapolation.

4.4 Comparisons between different MBIR methods

In sparse-view CT using 12.5% of the full projection views, the proposed Momentum-Net achieves significantly better reconstruction quality compared to the conventional EP MBIR method and the state-of-the-art MBIR method within an unsupervised learning setup, MBIR model using a learned convolutional regularizer [24], [37]. See Fig. 5(c)–(e) and Table S.1(b)–(e). In particular, Momentum-Net recovers both low- and high-contrast regions (e.g., soft tissues and bones, respectively) more accurately than MBIR using a learned convolutional regularizer; see Fig. 5(d)–(e). In addition, when the parameter dimensions, i.e., R and K , of their convolutional autoencoders, are identical, Momentum-Net achieves much faster MBIR compared to MBIR using a learned convolutional regularizer; see Table S.1(c)–(d). (This result corresponds to that in [37].)

In LF photography using five focal sensors, regardless of scene parameters and camera settings, Momentum-Net consistently achieves significantly more accurate image recovery, compared to MBIR model using the state-of-the-art non-trained regularizer, 4D EP [47]. The effectiveness of Momentum-Net is more evident for a scene with less

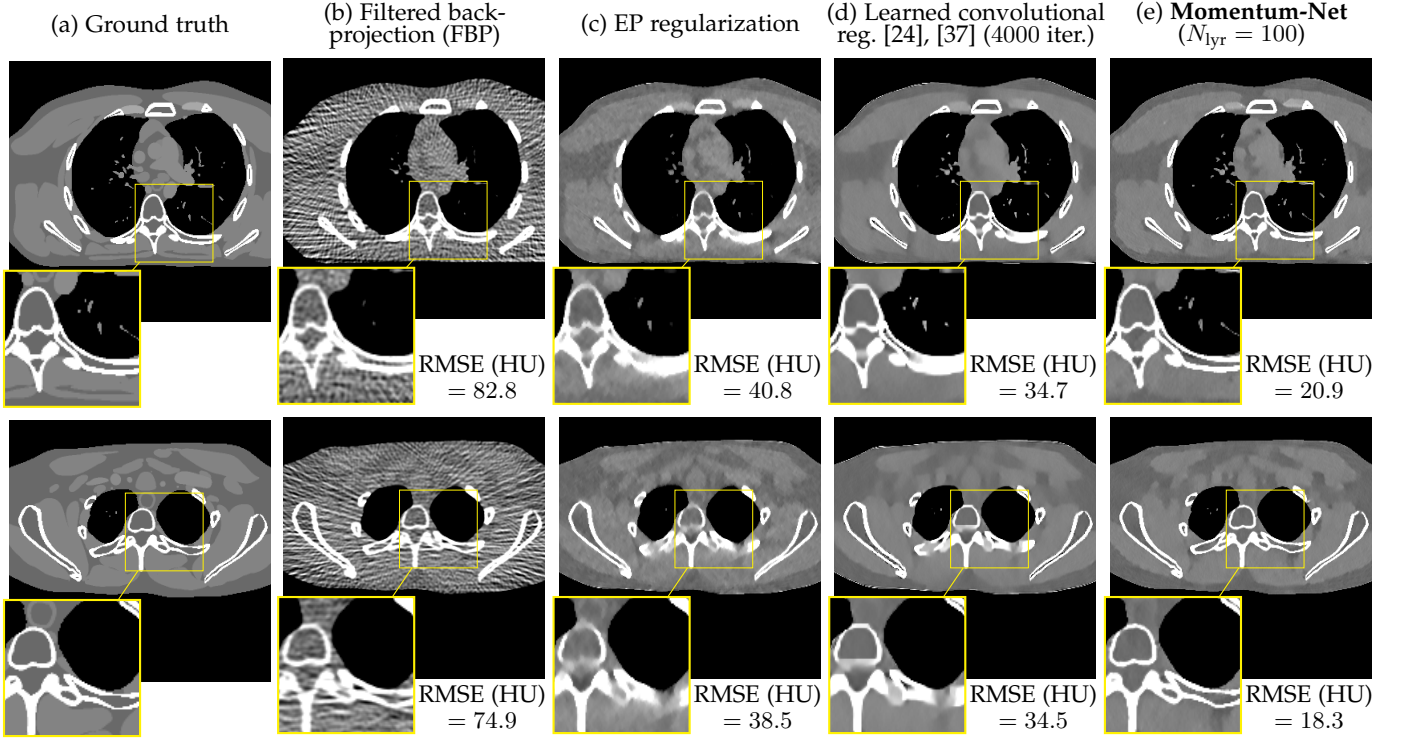


Fig. 5. Comparison of reconstructed images from different MBIR methods in sparse-view CT (fan-beam geometry with 12.5% projections views and 10^9 incident photons; images outside zoom-in boxes are magnified to better show differences; display window [800, 1200] HU).

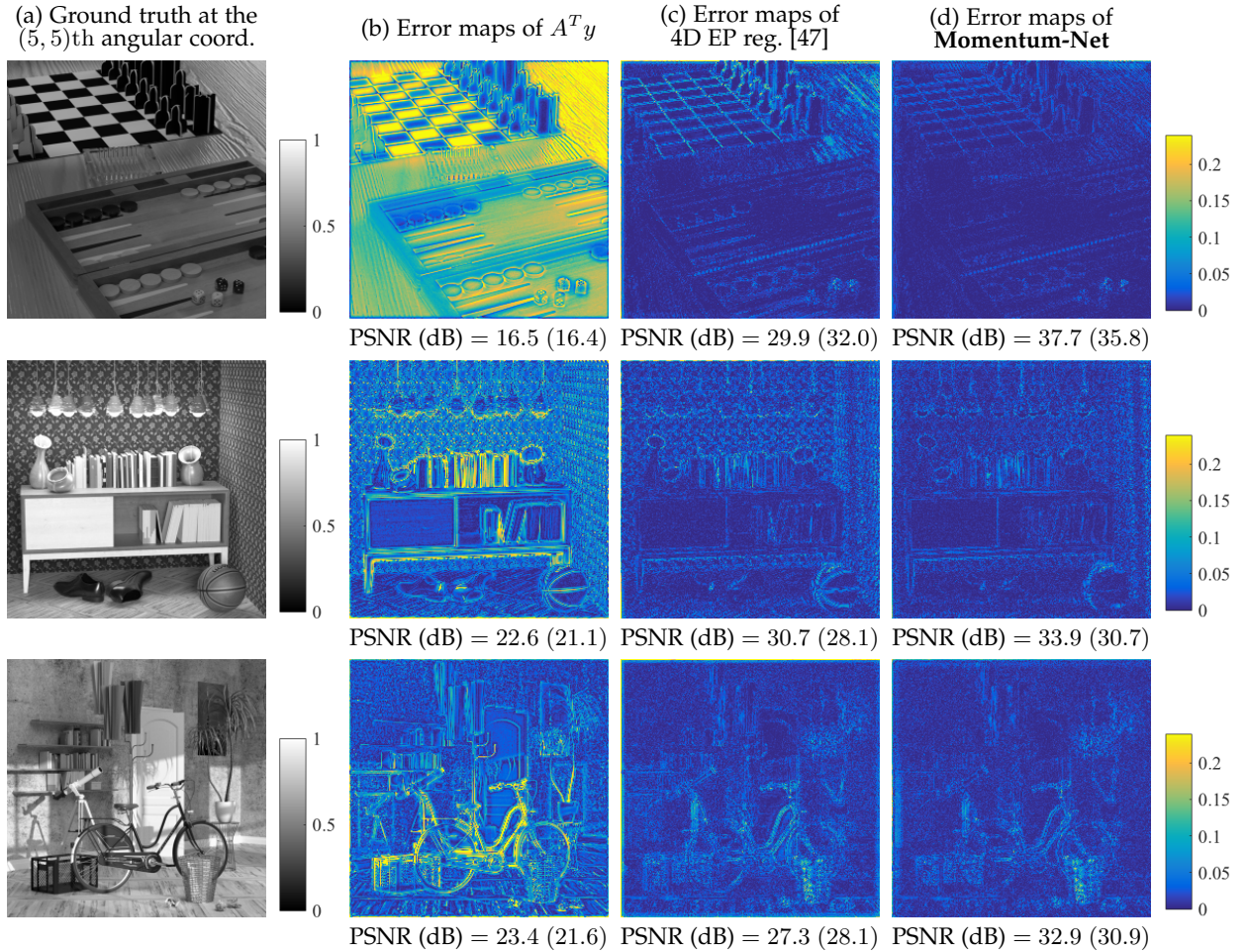


Fig. 6. Error map comparisons of reconstructed sub-aperture images from different MBIR methods in LF photography using focal stacks (LF photography systems with $C = 5$ detectors capture a focal stack of LFs consisting of $S = 81$ sub-aperture images; sub-aperture images at the (5, 5)th angular coordinate; the PSNR values in parenthesis were measured from reconstructed LFs).

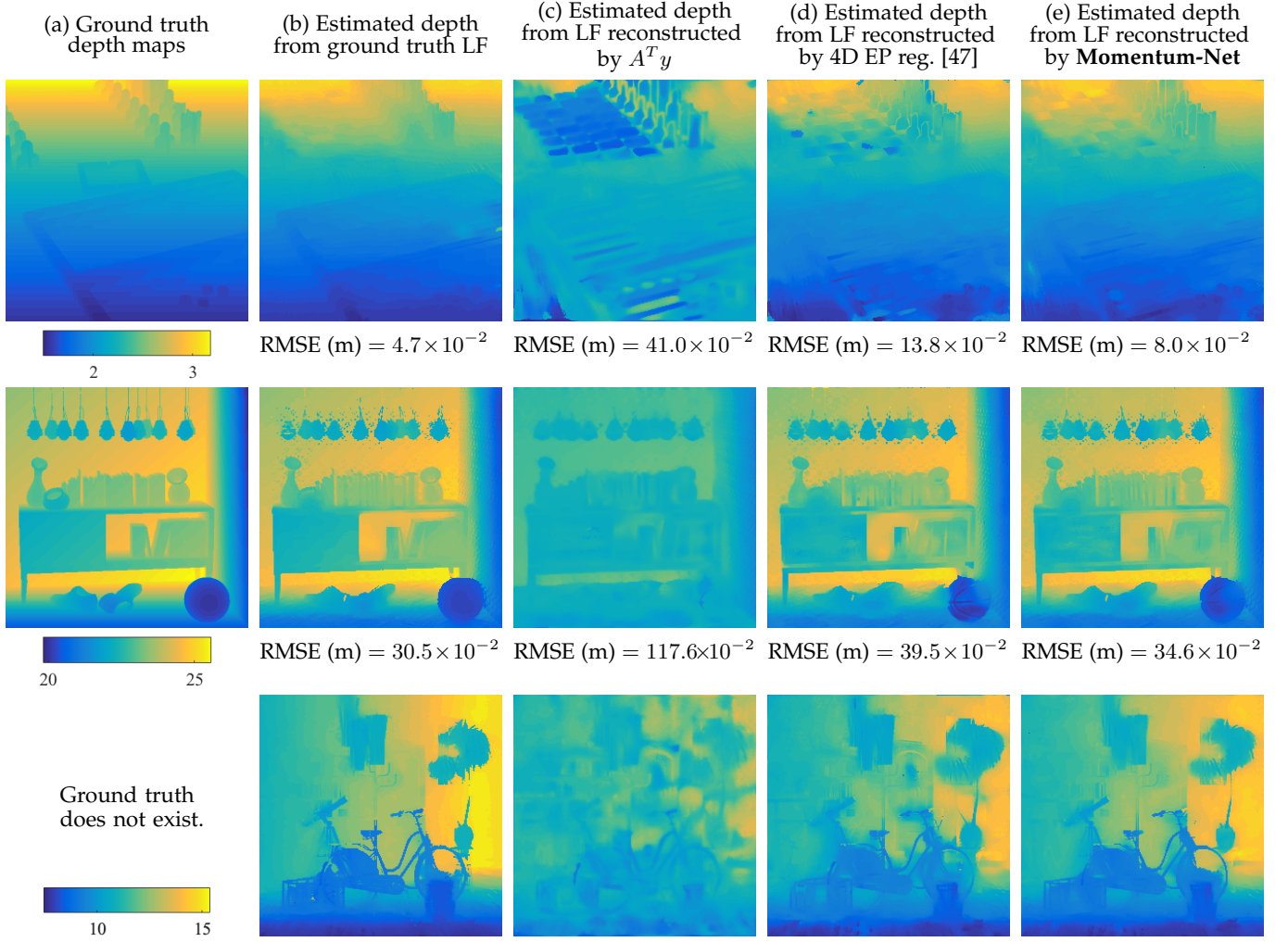


Fig. 7. Comparisons of estimated depths from LFs reconstructed by different MBIR methods in LF photograph using focal stacks (LF photography systems with $C = 5$ detectors capture a focal stack of LFs consisting of $S = 81$ sub-aperture images; SPO depth estimation [64] was applied to reconstructed LFs in Fig. 6; display window in meters).

fine details. See Fig. 6(c)–(d) and Table S.2(b)–(c). Regardless of the scene distances from LF imaging systems, the reconstructed LFs by Momentum-Net significantly improve the depth estimation accuracy over those reconstructed by the state-of-the-art non-trained regularizer, 4D EP [47]. See Fig. 7(d)–(e) and Table S.3(c)–(d).

5 CONCLUSIONS

Developing rapidly converging INNs is important, because 1) it leads to fast MBIR by reducing the computational complexity in calculating data-fit gradients or applying refining NNs, and 2) training INNs with many layers (or iterations) requires long training time or it is challenging when refining NNs are fixed across INN layers. The proposed Momentum-Net framework is applicable for a wide range of inverse problems, while achieving fast and convergent MBIR. To achieve fast MBIR, Momentum-Net uses momentum in extrapolation modules, and noniterative MBIR modules at each layer via majorizers. For sparse-view CT and LF photography using a focal stack, Momentum-Net achieves faster and more accurate MBIR compared to the existing INNs [21]–[23], [28], [30] that correspond to BCD-Net [25] or Momentum-Net using *no extrapolation*. In ad-

dition, Momentum-Net guarantees convergence to a fixed-point for general differentiable (non)convex MBIR functions (or data-fit terms) and convex feasible sets, under some mild conditions and two asymptotic conditions. The proposed regularization parameter selection scheme uses the spectral radius of majorization matrices, and is useful to consider data-fit variations across training and testing samples.

There are a number of avenues for future work. First, we expect to further improve performances of Momentum-Net (e.g., MBIR time and accuracy) by using sharper majorizer designs. Second, we expect to further reduce MBIR time of Momentum-Net with the stochastic gradient perspective (e.g., ordered subset [66]). On the regularization parameter selection side, our future work is learning the desired factor χ^* in (19) from datasets while training refining NNs.

APPENDIX A: NOTATION

We use $\|\cdot\|_p$ to denote the ℓ^p -norm and write $\langle \cdot, \cdot \rangle$ for the standard inner product on \mathbb{C}^N . The weighted ℓ^2 -norm with a Hermitian positive definite matrix A is denoted by $\|\cdot\|_A = \|A^{\frac{1}{2}}(\cdot)\|_2$. The Frobenius norm of a matrix is denoted by $\|\cdot\|_F$. $(\cdot)^T$, $(\cdot)^H$, and $(\cdot)^*$ indicate the transpose, complex conjugate transpose (Hermitian transpose),

Algorithm 2 BCD-Net [25]

Require: $\{\mathcal{R}_{\theta^{(i)}} : i = 1, \dots, N_{\text{lyr}}\}, \gamma > 0, x^{(0)} = x^{(-1)}, y$
for $i = 0, \dots, N_{\text{lyr}} - 1$ **do**
 Image refining:

$$z^{(i+1)} = \mathcal{R}_{\theta^{(i+1)}}(x^{(i)}) \quad (\text{Alg.2.1})$$

 MBIR:

$$x^{(i+1)} = \underset{x \in \mathcal{X}}{\operatorname{argmin}} F(x; y, z^{(i+1)}) \quad (\text{Alg.2.2})$$

end for

and complex conjugate, respectively. $\operatorname{diag}(\cdot)$ denotes the conversion of a vector into a diagonal matrix or diagonal elements of a matrix into a vector. For (self-adjoint) matrices $A, B \in \mathbb{C}^{N \times N}$, the notation $B \preceq A$ denotes that $A - B$ is a positive semi-definite matrix.

APPENDIX B: MOMENTUM-NET VS. BCD-NET

This section compares the convergence properties of Momentum-Net (Algorithm 1) and BCD-Net (Algorithm 2). We first show that for convex $f(x; y)$ and \mathcal{X} , the sequence of reconstructed images generated by BCD-Net converges:

Proposition 14 (Sequence convergence). *In Algorithm 2, let $f(x; y)$ be convex and subdifferentiable, and \mathcal{X} be convex. Assume that the paired operators $(\mathcal{R}_{\theta^{(i+1)}}, \mathcal{R}_{\theta^{(i)}})$ are asymptotically contractive, i.e.,*

$$\|\mathcal{R}_{\theta^{(i+1)}}(u) - \mathcal{R}_{\theta^{(i)}}(v)\|_2 < \|u - v\|_2 + \epsilon^{(i+1)},$$

with $\sum_{i=0}^{\infty} \epsilon^{(i+1)} < \infty$ and $\{\epsilon^{(i+1)} \in [0, \infty) : \forall i\}, \forall u, v, i$. Then, the sequence $\{x^{(i+1)} : i \geq 0\}$ generated by Algorithm 2 is convergent.

Proof. See §S.6 of the supplementary material.

In terms of guaranteeing convergence, BCD-Net has three theoretical or practical limitations compared to Momentum-Net:

- Different from Momentum-Net, BCD-Net assumes the asymptotic contractive property for the paired operators $\{\mathcal{R}_{\theta^{(i+1)}}, \mathcal{R}_{\theta^{(i)}}\}$. When image mapping operators in (Alg.2.1) are identical across layers, i.e., $\{\mathcal{R}_{\theta} = \mathcal{R}_{\theta^{(i+1)}} : i \geq 0\}$, then \mathcal{R}_{θ} is assumed to be contractive. On the other hand, a mapping operator (identical across layers) of Momentum-Net only needs to be nonexpansive. Note, however, that when $f(x; y) = \frac{1}{2}\|y - Ax\|_W^2$ with $A^H W A \succ 0$ (e.g., Example 5), BCD-Net can guarantee the sequence convergence with the asymptotically non-expansive paired operators $(\mathcal{R}_{\theta^{(i+1)}}, \mathcal{R}_{\theta^{(i)}})$ (see Definition 9) [17].
- When one applies an iterative solver to (Alg.2.2), there always exist some numerical errors and these obstruct the sequence convergence guarantee in Proposition 14. To guarantee sufficiently small numerical errors from iterative methods solving (Alg.2.2) (so that one can find a critical point solution for the MBIR problem (Alg.2.2)), one needs to use sufficiently many iterations; which can be slow. can substantially slow down entire MBIR.
- BCD-Net does not guarantee the sequence convergence for nonconvex data-fit $f(x; y)$, whereas Momentum-Net guarantees convergence to a fixed-point for both convex $f(x; y)$ and nonconvex $f(x; y)$.

REFERENCES

- [1] P. Vincent, H. Larochelle, I. Lajoie, Y. Bengio, and P.-A. Manzagol, "Stacked denoising autoencoders: Learning useful representations in a deep network with a local denoising criterion," *J. Mach. Learn. Res.*, vol. 11, no. Dec, pp. 3371–3408, 2010.
- [2] J. Xie, L. Xu, and E. Chen, "Image denoising and inpainting with deep neural networks," in *Proc. NIPS* 25, Lake Tahoe, NV, Dec. 2012, pp. 341–349.
- [3] X. Mao, C. Shen, and Y.-B. Yang, "Image restoration using very deep convolutional encoder-decoder networks with symmetric skip connections," in *Proc. NIPS* 29, Barcelona, Spain, Dec. 2016, pp. 2802–2810.
- [4] K. Zhang, W. Zuo, Y. Chen, D. Meng, and L. Zhang, "Beyond a Gaussian denoiser: Residual learning of deep CNN for image denoising," *IEEE Trans. Image Process.*, vol. 26, no. 7, pp. 3142–3155, Feb. 2017.
- [5] L. Xu, J. S. Ren, C. Liu, and J. Jia, "Deep convolutional neural network for image deconvolution," in *Proc. NIPS* 27, Montreal, Canada, Dec. 2014, pp. 1790–1798.
- [6] J. Sun, W. Cao, Z. Xu, and J. Ponce, "Learning a convolutional neural network for non-uniform motion blur removal," in *Proc. IEEE CVPR*, Boston, MA, Jun. 2015, pp. 769–777.
- [7] C. Dong, C. C. Loy, K. He, and X. Tang, "Image super-resolution using deep convolutional networks," *IEEE Trans. Pattern Anal. Mach. Intell.*, vol. 38, no. 2, pp. 295–307, Feb. 2016.
- [8] J. Kim, K. J. Lee, and K. M. Lee, "Accurate image super-resolution using very deep convolutional networks," in *Proc. IEEE CVPR*, Las Vegas, NV, Jun. 2016.
- [9] G. Yang, S. Yu, H. Dong, G. Slabaugh, P. L. Dragotti, X. Ye, F. Liu, S. Arridge, J. Keegan, Y. Guo *et al.*, "DAGAN: Deep de-aliasing generative adversarial networks for fast compressed sensing MRI reconstruction," *IEEE Trans. Image Process.*, vol. 37, no. 6, pp. 1310–1321, Jun. 2018.
- [10] T. M. Quan, T. Nguyen-Duc, and W. Jeong, "Compressed sensing MRI reconstruction using a generative adversarial network with a cyclic loss," *IEEE Trans. Med. Imag.*, vol. 37, no. 6, pp. 1488–1497, June 2018.
- [11] H. Chen, Y. Zhang, M. K. Kalra, F. Lin, P. Liao, J. Zhou, and G. Wang, "Low-dose CT with a residual encoder-decoder convolutional neural network (RED-CNN)," *IEEE Trans. Med. Imag.*, vol. PP, no. 99, p. 0, Jun. 2017.
- [12] K. H. Jin, M. T. McCann, E. Froustey, and M. Unser, "Deep convolutional neural network for inverse problems in imaging," *IEEE Trans. Image Process.*, vol. 26, no. 9, pp. 4509–4522, Sep. 2017.
- [13] J. Ye, Y. Han, and E. Cha, "Deep convolutional framelets: A general deep learning framework for inverse problems," *SIAM J. Imaging Sci.*, vol. 11, no. 2, pp. 991–1048, Apr. 2018.
- [14] G. Wu, M. Zhao, L. Wang, Q. Dai, T. Chai, and Y. Liu, "Light field reconstruction using deep convolutional network on EPI," in *Proc. IEEE CVPR*, Honolulu, HI, Jul. 2017, pp. 1638–1646.
- [15] M. Gupta, A. Jauhari, K. Kulkarni, S. Jayasuriya, A. C. Molnar, and P. K. Turaga, "Compressive light field reconstructions using deep learning," in *Proc. IEEE CVPR Workshops*, Honolulu, HI, Jul. 2017, pp. 1277–1286.
- [16] G. Wang, J. C. Ye, K. Mueller, and J. A. Fessler, "Image reconstruction is a new frontier of machine learning," *IEEE Trans. Med. Imag.*, vol. 37, no. 6, pp. 1289–1296, Jun. 2018.
- [17] I. Y. Chun, X. Zheng, Y. Long, and J. A. Fessler, "BCD-Net for low-dose CT reconstruction: Acceleration, convergence, and generalization," in *Proc. Med. Image Compt. and Computer Assist. Inte. (MICCAI)* (accepted), Jul. 2019.
- [18] X. Zheng, I. Y. Chun, Z. Li, Y. Long, and J. A. Fessler, "Sparse-view X-ray CT reconstruction using ℓ_1 prior with learned transform," submitted, Feb. 2019. [Online]. Available: <http://arxiv.org/abs/1711.00905>
- [19] H. Lim, I. Y. Chun, Y. K. Dewaraja, and J. A. Fessler, "Improved low-count quantitative PET reconstruction with a variational neural network," submitted, May 2019. [Online]. Available: <http://arxiv.org/abs/1906.02327>
- [20] Y. Yang, J. Sun, H. Li, and Z. Xu, "Deep ADMM-Net for compressive sensing MRI," in *Proc. NIPS* 29, Long Beach, CA, Dec. 2016, pp. 10–18.
- [21] Y. Chen and T. Pock, "Trainable nonlinear reaction diffusion: A flexible framework for fast and effective image restoration," *IEEE Trans. Pattern Anal. Mach. Intell.*, vol. 39, no. 6, pp. 1256–1272, Jun. 2017.

- [22] Y. Romano, M. Elad, and P. Milanfar, "The little engine that could: Regularization by denoising (RED)," *SIAM J. Imaging Sci.*, vol. 10, no. 4, pp. 1804–1844, Oct. 2017.
- [23] G. T. Buzzard, S. H. Chan, S. Sreehari, and C. A. Bouman, "Plug-and-play unplugged: Optimization free reconstruction using consensus equilibrium," *SIAM J. Imaging Sci.*, vol. 11, no. 3, pp. 2001–2020, Sep. 2018.
- [24] I. Y. Chun and J. A. Fessler, "Convolutional analysis operator learning: Acceleration and convergence," submitted, Jan. 2019. [Online]. Available: <http://arxiv.org/abs/1802.05584>
- [25] —, "Deep BCD-net using identical encoding-decoding CNN structures for iterative image recovery," in *Proc. IEEE IVMSWP Workshop*, Zagori, Greece, Jun. 2018, pp. 1–5.
- [26] M. Mardani, Q. Sun, D. Donoho, V. Pappayan, H. Monajemi, S. Vasanawala, and J. Pauly, "Neural proximal gradient descent for compressive imaging," in *Proc. NIPS 31*, Montreal, Canada, Dec. 2018, pp. 9573–9583.
- [27] I. Y. Chun, H. Lim, Z. Huang, and J. A. Fessler, "Fast and convergent iterative signal recovery using trained convolutional neural networks," in *Proc. Allerton Conf. on Commun., Control, and Comput.*, Allerton, IL, Oct. 2018, pp. 155–159.
- [28] K. Hammernik, T. Klatzer, E. Kobler, M. P. Recht, D. K. Sodickson, T. Pock, and F. Knoll, "Learning a variational network for reconstruction of accelerated MRI data," *Magn. Reson. Med.*, vol. 79, no. 6, pp. 3055–3071, Nov. 2017.
- [29] M. Mardani, E. Gong, J. Y. Cheng, S. S. Vasanawala, G. Zaharchuk, L. Xing, and J. M. Pauly, "Deep generative adversarial neural networks for compressive sensing (GANCS) MRI," *IEEE Trans. Med. Imag.*, 2018.
- [30] H. K. Aggarwal, M. P. Mani, and M. Jacob, "MoDL: Model based deep learning architecture for inverse problems," *IEEE Trans. Med. Imag.*, vol. 38, no. 2, pp. 394–405, Feb. 2019.
- [31] H. Gupta, K. H. Jin, H. Q. Nguyen, M. T. McCann, and M. Unser, "CNN-based projected gradient descent for consistent CT image reconstruction," *IEEE Trans. Med. Imag.*, vol. 37, no. 6, pp. 1440–1453, Jun. 2018.
- [32] K. Kim, D. Wu, K. Gong, J. Dutta, J. H. Kim, Y. D. Son, H. K. Kim, G. El Fakhri, and Q. Li, "Penalized PET reconstruction using deep learning prior and local linear fitting," *IEEE Trans. Med. Imag.*, vol. 37, no. 6, pp. 1478–1487, Jun. 2018.
- [33] H. Lim, J. A. Fessler, Y. K. Dewaraja, and I. Y. Chun, "Application of trained Deep BCD-Net to iterative low-count PET image reconstruction," in *Proc. IEEE NSS-MIC* (to appear), Sydney, Australia, Nov. 2018.
- [34] H. Lim, I. Y. Chun, J. A. Fessler, and Y. K. Dewaraja, "Improved low count quantitative SPECT reconstruction with a trained deep learning based regularizer," in *Proc. Soc. Nucl. Med. & Mol. Imag. (SNMMI)* (to appear), Anaheim, CA, Jun. 2019.
- [35] I. Y. Chun and J. A. Fessler, "Convolutional dictionary learning: Acceleration and convergence," *IEEE Trans. Image Process.*, vol. 27, no. 4, pp. 1697–1712, Apr. 2018.
- [36] I. Y. Chun, D. Hong, B. Adcock, and J. A. Fessler, "Convolutional analysis operator learning: Dependence on training data and compressed sensing recovery guarantees," to appear in *IEEE Signal Process. Lett.*, Jun. 2019. [Online]. Available: <http://arxiv.org/abs/1902.08267>
- [37] I. Y. Chun and J. A. Fessler, "Convolutional analysis operator learning: Application to sparse-view CT," in *Proc. Asilomar Conf. on Signals, Syst., and Comput.*, Pacific Grove, CA, Oct. 2018, pp. 1631–1635.
- [38] S. Sreehari, S. V. Venkatakrishnan, B. Wohlberg, G. T. Buzzard, L. F. Drummy, J. P. Simmons, and C. A. Bouman, "Plug-and-play priors for bright field electron tomography and sparse interpolation," *IEEE Trans. Comput. Imag.*, vol. 2, no. 4, pp. 408–423, Aug. 2016.
- [39] K. Zhang, W. Zuo, S. Gu, and L. Zhang, "Learning deep CNN denoiser prior for image restoration," in *Proc. IEEE CVPR*, Honolulu, HI, Jul. 2017, pp. 4681–4690.
- [40] S. H. Chan, X. Wang, and O. A. Elgendy, "Plug-and-play ADMM for image restoration: Fixed-point convergence and applications," *IEEE Trans. Comput. Imag.*, vol. 3, no. 1, pp. 84–98, Nov. 2017.
- [41] S. Boyd, N. Parikh, E. Chu, B. Peleato, and J. Eckstein, "Distributed optimization and statistical learning via the alternating direction method of multipliers," *Found. & Trends in Machine Learning*, vol. 3, no. 1, pp. 1–122, Jan. 2011.
- [42] E. T. Reehorst and P. Schniter, "Regularization by denoising: Clarifications and new interpretations," *IEEE Trans. Comput. Imag.*, vol. 5, no. 1, pp. 52–67, Mar. 2019.
- [43] U. S. Kamilov, H. Mansour, and B. Wohlberg, "A plug-and-play priors approach for solving nonlinear imaging inverse problems," *IEEE Signal Process. Lett.*, vol. 24, no. 12, pp. 1872–1876, Dec. 2017.
- [44] Y. Nesterov, "Gradient methods for minimizing composite functions," *Math. Program.*, vol. 140, no. 1, pp. 125–161, Aug. 2013.
- [45] A. Beck and M. Teboulle, "A fast iterative shrinkage-thresholding algorithm for linear inverse problems," *SIAM J. Imaging Sci.*, vol. 2, no. 1, pp. 183–202, Mar. 2009.
- [46] K. Dabov, A. Foi, V. Katkovnik, and K. Egiazarian, "Image denoising by sparse 3-d transform-domain collaborative filtering," *IEEE Trans. Image Process.*, vol. 16, no. 8, pp. 2080–2095, Jul. 2007.
- [47] C. J. Blocker, I. Y. Chun, and J. A. Fessler, "Low-rank plus sparse tensor models for light-field reconstruction from focal stack data," in *Proc. IEEE IVMSWP Workshop*, Zagori, Greece, Jun. 2018, pp. 1–5.
- [48] I. Y. Chun and B. Adcock, "Compressed sensing and parallel acquisition," *IEEE Trans. Inf. Theory*, vol. 63, no. 7, pp. 1–23, May 2017. [Online]. Available: <http://arxiv.org/abs/1601.06214>
- [49] S. Aja-Fernández, G. Vegas-Sánchez-Ferrero, and A. Tristán-Vega, "Noise estimation in parallel MRI: GRAPPA and SENSE," *Magn. Reson. Imaging*, vol. 32, no. 3, pp. 281–290, Apr. 2014.
- [50] R. T. Rockafellar, "Monotone operators and the proximal point algorithm," *SIAM J. Control Optim.*, vol. 14, no. 5, pp. 877–898, Aug. 1976.
- [51] E. K. Ryu and S. Boyd, "Primer on monotone operator methods," *Appl. Comput. Math.*, vol. 15, no. 1, pp. 3–43, Jan. 2016.
- [52] Y. Xu and W. Yin, "A block coordinate descent method for regularized multiconvex optimization with applications to nonnegative tensor factorization and completion," *SIAM J. Imaging Sci.*, vol. 6, no. 3, pp. 1758–1789, Sep. 2013.
- [53] J. Bolte, S. Sabach, and M. Teboulle, "Proximal alternating linearized minimization or nonconvex and nonsmooth problems," *Math. Program.*, vol. 146, no. 1–2, pp. 459–494, Aug. 2014.
- [54] Y. Xu and W. Yin, "A globally convergent algorithm for nonconvex optimization based on block coordinate update," *J. Sci. Comput.*, vol. 72, no. 2, pp. 700–734, Aug. 2017.
- [55] K. He, X. Zhang, S. Ren, and J. Sun, "Deep residual learning for image recognition," in *Proc. IEEE CVPR*, Las Vegas, NV, June 2016.
- [56] H. Li, Z. Xu, G. Taylor, C. Studer, and T. Goldstein, "Visualizing the loss landscape of neural nets," in *Proc. NIPS 31*, Montreal, Canada, Dec. 2018, pp. 6389–6399.
- [57] I. Y. Chun and T. Talavage, "Efficient compressed sensing statistical X-ray/CT reconstruction from fewer measurements," in *Proc. Intl. Mtg. on Fully 3D Image Recon. in Rad. and Nuc. Med.*, Lake Tahoe, CA, Jun. 2013, pp. 30–33.
- [58] D. Zhang, Z. Xu, Z. Huang, A. R. Gutierrez, I. Y. Chun, C. J. Blocker, G. Cheng, Z. Liu, J. A. Fessler, Z. Zhong, and T. B. Norris, "Graphene-based transparent photodetector array for multiplane imaging," in *Proc. Conf. on Lasers and Electro-Optics*, San Jose, CA, May 2019, p. SM4J.2.
- [59] K. Honauer, O. Johannsen, D. Kondermann, and B. Goldluecke, "A dataset and evaluation methodology for depth estimation on 4D light fields," in *Proc. ACCV*, Taipei, Taiwan, Nov. 2016, pp. 19–34.
- [60] W. P. Segars, M. Mahesh, T. J. Beck, E. C. Frey, and B. M. Tsui, "Realistic CT simulation using the 4D XCAT phantom," *Med. Phys.*, vol. 35, no. 8, pp. 3800–3808, Jul. 2008.
- [61] D. P. Kingma and J. L. Ba, "Adam: A method for stochastic optimization," in *Proc. ICLR 2015*, San Diego, CA, May 2015, pp. 1–15.
- [62] K. He, X. Zhang, S. Ren, and J. Sun, "Delving deep into rectifiers: Surpassing human-level performance on ImageNet classification," in *Proc. IEEE ICCV*, Santiago, Chile, Dec. 2015, pp. 1026–1034.
- [63] M. H. Kamal, B. Heshmat, R. Raskar, P. Vanderghenst, and G. Wetzstein, "Tensor low-rank and sparse light field photography," *Comput. Vis. Image Und.*, vol. 145, pp. 172–181, Apr. 2016.
- [64] S. Zhang, H. Sheng, C. Li, J. Zhang, and Z. Xiong, "Robust depth estimation for light field by spinning parallelogram operator," *Comput. Vis. Image Und.*, vol. 145, pp. 148–159, Apr. 2016.
- [65] J. A. Fessler, "Michigan image reconstruction toolbox (MIRT) for Matlab," 2016, available from <http://web.eecs.umich.edu/~fessler>.
- [66] H. Erdogan and J. A. Fessler, "Ordered subsets algorithms for transmission tomography," *Phys. Med. Biol.*, vol. 44, no. 11, p. 2835, Jul. 1999.

Momentum-Net: Fast and convergent iterative neural network for inverse problems (Supplementary material)

This supplementary material for [1] reviews the Block Proximal Extrapolated Gradient method using a Majorizer (BPEG-M) [2], [3], and provides mathematical proofs or detailed descriptions to support several arguments in the main manuscript. We use the prefix “S” for the numbers in section, theorem, equation, figure, table, and footnote in the supplement.^{S.1}

S.1 BPEG-M: REVIEW

This section explains *block multi-(non)convex* optimization problems, and summarizes the state-of-the-art method for block multi-(non)convex optimization, BPEG-M [2], [3], along with its convergence guarantees.

S.1.1 Block multi-(non)convex optimization

In a block optimization problem, the variables of the underlying optimization problem are treated either as a single block or multiple disjoint blocks. In *block multi-(non)convex* optimization, we consider the following problem:

$$\min_u F(u_1, \dots, u_B) := f(u_1, \dots, u_B) + \sum_{b=1}^B r_b(u_b) \quad (\text{S.1})$$

where variable u is decomposed into B blocks u_1, \dots, u_B ($\{u_b \in \mathbb{R}^{n_b} : b = 1, \dots, B\}$), f is assumed to be (continuously) differentiable, but functions $\{r_b : b = 1, \dots, B\}$ are not necessarily differentiable. The function r_b can incorporate the constraint $u_b \in \mathcal{U}_b$, by allowing r_b 's to be extended-valued, e.g., $r_b(u_b) = \infty$ if $u_b \notin \mathcal{U}_b$, for $b = 1, \dots, B$. It is standard to assume that both f and $\{r_b\}$ are proper and closed, and the sets $\{\mathcal{U}_b\}$ are closed. We consider either that (S.1) has block-wise convexity (but (S.1) is jointly nonconvex in general) [2], [4] or that f , $\{r_b\}$, or $\{\mathcal{U}_b\}$ are not necessarily convex [3], [5]. Importantly, r_b can include (non)convex and nonsmooth ℓ^p (quasi-)norm, $p \in [0, 1]$. The next section introduces our optimization framework that solves (S.1).

The following sections review BPEG-M [2], [3], the state-of-the-art optimization framework for solving block multi-(non)convex problems, when used with sufficiently sharp majorizers. BPEG-M uses block-wise extrapolation, majorization, and proximal mapping. By using a more general Lipschitz continuity (see Definition 1) for block-wise gradients, BPEG-M is particularly useful for rapidly calculating majorizers involved with large-scale problems, and successfully applied to some large-scale machine learning and computational imaging problems; see [2], [3], [6] and references therein.

S.1.2 BPEG-M

This section summarizes the BPEG-M framework. Using Definition 1 and Lemma 2, the proposed method, BPEG-M, is given as follows. To solve (S.1), we minimize majorizers of F cyclically over each block u_1, \dots, u_B , while fixing the remaining blocks at their previously updated variables. Let $u_b^{(i+1)}$ be the value of u_b after its i th update, and define

$$f_b^{(i+1)}(u_b) := f(u_1^{(i+1)}, \dots, u_{b-1}^{(i+1)}, u_b, u_{b+1}^{(i)}, \dots, u_B^{(i)}),$$

for all b, i . At the b th block of the i th iteration, we apply Lemma 2 to functional $f_b^{(i+1)}(u_b)$ with a $M^{(i+1)}$ -Lipschitz continuous gradient at the extrapolated point $\hat{u}_b^{(i+1)}$, and minimize a majorized function. In other words, we consider the updates

$$\begin{aligned} u_b^{(i+1)} &= \operatorname{argmin}_{u_b} \langle \nabla f_b^{(i+1)}(\hat{u}_b^{(i+1)}), u_b - \hat{u}_b^{(i+1)} \rangle + \frac{1}{2} \|u_b - \hat{u}_b^{(i+1)}\|_{\widetilde{M}_b^{(i+1)}}^2 + r_b(u_b) \\ &= \operatorname{Prox}_{r_b}^{\widetilde{M}_b^{(i+1)}} \left(\underbrace{\hat{u}_b^{(i+1)} - (\widetilde{M}_b^{(i+1)})^{-1} \nabla f_b^{(i+1)}(\hat{u}_b^{(i+1)})}_{\text{extrapolated gradient step using a majorizer of } f_b^{(i+1)}} \right), \end{aligned} \quad (\text{S.2})$$

where

$$\hat{u}_b^{(i+1)} = u_b^{(i)} + E_b^{(i+1)}(u_b^{(i)} - u_b^{(i-1)}), \quad (\text{S.3})$$

Algorithm S.1 BPEG-M [2], [3]

Require: $\{u_b^{(0)} = u_b^{(-1)} : \forall b\}$, $\{w_b^{(i)} \in [0, 1], \forall b, i\}$, $i = 0$
while a stopping criterion is not satisfied **do**
 for $b = 1, \dots, B$ **do**
 Calculate $\widetilde{M}_b^{(i+1)}$ by (S.4), and $E_b^{(i+1)}$ to satisfy (S.5) or (S.6)
 $\hat{u}_b^{(i+1)} = u_b^{(i)} + E_b^{(i+1)}(u_b^{(i)} - u_b^{(i-1)})$
 $u_b^{(i+1)} = \text{Prox}_{r_b}^{\widetilde{M}_b^{(i+1)}}\left(u_b^{(i+1)} - \left(\widetilde{M}_b^{(i+1)}\right)^{-1} \nabla f_b^{(i+1)}(\hat{u}_b^{(i+1)})\right)$
 end for
 $i = i + 1$
end while

the proximal operator is defined by (2), $\nabla f_b^{(i+1)}(\hat{u}_b^{(i+1)})$ is the block-partial gradient of f at $\hat{u}_b^{(i+1)}$, a *scaled majorization matrix* is given by

$$\widetilde{M}_b^{(i+1)} = \lambda_b \cdot M_b^{(i+1)} \succ 0, \quad \lambda_b \geq 1, \quad (\text{S.4})$$

and $M_b^{(i+1)} \in \mathbb{R}^{n_b \times n_b}$ is a symmetric positive definite *majorization matrix* of $\nabla f_b^{(i+1)}(u_b)$. In (S.3), the $\mathbb{R}^{n_b \times n_b}$ matrix $E_b^{(i+1)} \succeq 0$ is an *extrapolation matrix* that accelerates convergence in solving block multi-convex problems [2]. We design it to satisfy conditions (S.5) or (S.6) below. In (S.4), $\{\lambda_b = 1 : \forall b\}$ and $\{\lambda_b > 1 : \forall b\}$, for block multi-convex and block multi-nonconvex problems, respectively.

For some $f_b^{(i+1)}$ having sharp majorizers, we expect that extrapolation (S.3) has no benefits in accelerating convergence, and use $\{E_b^{(i+1)} = 0 : \forall i\}$. Other than the blocks having sharp majorizers, one can apply some increasing momentum coefficient formula [7], [8] to the corresponding extrapolation matrices. The choice in [2]–[4] accelerated BPEG-M for some machine learning and data science applications. Algorithm S.1 summarizes these updates.

S.1.3 Convergence results

This section summarizes convergence results of Algorithm S.1 under the following assumptions:

- *Assumption S.1*) In (S.1), F is proper and lower bounded in $\text{dom}(F) := \{u : F(u) < \infty\}$. In addition,
 for *block multi-convex* (S.1), f is differentiable and (S.1) has a Nash point or block-coordinate minimizer^{S.2} (see its definition in [4, (2.3)–(2.4)]);
 for *block multi-nonconvex* (S.1), f is continuously differentiable, r_b is lower semicontinuous^{S.3}, $\forall b$, and (S.1) has a critical point u^* that satisfies $0 \in \partial F(u^*)$.
- *Assumption S.2*) $\nabla f_b^{(i+1)}(u_b)$ is M -Lipschitz continuous with respect to u_b , i.e.,

$$\left\| \nabla f_b^{(i+1)}(u) - \nabla f_b^{(i+1)}(v) \right\|_{(M_b^{(i+1)})^{-1}} \leq \|u - v\|_{M_b^{(i+1)}},$$

for $u, v \in \mathbb{R}^{n_b}$, where $M_b^{(i+1)}$ is a bounded majorization matrix.

- *Assumption S.3*) The extrapolation matrices $E_b^{(i+1)} \succeq 0$ satisfy that

$$\text{for block multi-convex (S.1), } (E_b^{(i+1)})^T M_b^{(i+1)} E_b^{(i+1)} \preceq \delta^2 \cdot M_b^{(i)}; \quad (\text{S.5})$$

$$\text{for block multi-nonconvex (S.1), } (E_b^{(i+1)})^T M_b^{(i+1)} E_b^{(i+1)} \preceq \frac{\delta^2(\lambda_b - 1)^2}{4(\lambda_b + 1)^2} \cdot M_b^{(i)}, \quad (\text{S.6})$$

with $\delta < 1, \forall b, i$.

Theorem S.1 (*Block multi-convex* (S.1): A limit point is a Nash point [2]). *Under Assumptions S.1–S.3, let $\{u^{(i+1)} : i \geq 0\}$ be the sequence generated by Algorithm S.1. Then any limit point of $\{u^{(i+1)} : i \geq 0\}$ is a Nash point of (S.1).*

Theorem S.2 (*Block multi-nonconvex* (S.1): A limit point is a critical point [3]). *Under Assumptions S.1–S.3, let $\{u^{(i+1)} : i \geq 0\}$ be the sequence generated by Algorithm S.1. Then any limit point of $\{u^{(i+1)} : i \geq 0\}$ is a critical point of (S.1).*

Remark S.3. Theorems S.1–S.2 imply that, if there exists a critical point for (S.1), i.e., $0 \in \partial F(u^*)$, then any limit point of $\{u^{(i+1)} : i \geq 0\}$ is a critical point. One can further show global convergence under some conditions: if $\{u^{(i+1)} : i \geq 0\}$ is bounded and the critical points are isolated, then $\{u^{(i+1)} : i \geq 0\}$ converges to a critical point [2, Rem. 3.4], [4, Cor. 2.4].

S.1.4 Application of BPEG-M to solving block multi-(non)convex problem (1)

For update (3), we do not use extrapolation, i.e., (S.3), since the corresponding majorization matrices are sharp, so one obtains tight majorization bounds in Lemma 2. See, for example, [3, §V-B]. For updates (3) and (5), we rewrite $\sum_{k=1}^K \|h_k * x - \zeta_k\|_2^2$ as $\|x - \sum_{k=1}^K \text{flip}(h_k^*) * \zeta_k\|_2^2$ by using the TF condition in §2.1 [3, §VI], [6].

S.2. Given a feasible set \mathcal{U} , a point $u^* \in \text{dom}(F) \cup \mathcal{U}$ is a critical point (or stationary point) of F if the directional derivative $d^T \nabla F(u^*) \geq 0$ for any feasible direction d at u^* . If u^* is an interior point of \mathcal{U} , then the condition is equivalent to $0 \in \partial F(u^*)$.

S.3. F is lower semicontinuous at point u_0 if $\liminf_{u \rightarrow u_0} F(u) \geq F(u_0)$.

S.2 PROBABILISTIC JUSTIFICATION FOR THE ASYMPTOTIC BLOCK-COORDINATE MINIMIZER CONDITION IN ASSUMPTION 4

This section introduces a useful result for an asymptotic block-coordinate minimizer $z^{(i+1)}$: the following lemma provides a *probabilistic* bound for $\|x^{(i)} - z^{(i+1)}\|_2^2$ in (12), given a subgaussian vector $z^{(i+1)} - z^{(i)}$ with independent and zero-mean entries.

Lemma S.4 (Probabilistic bounds for $\|x^{(i)} - z^{(i+1)}\|_2^2$). *Assume that $z^{(i+1)} - z^{(i)}$ is a zero-mean subgaussian vector of which entries are independent and zero-mean subgaussian variables. Then, each bound in (12) holds with probability at least*

$$1 - \exp\left(-\frac{\left(\|z^{(i+1)} - z^{(i)}\|_2^2 + \Delta^{(i+1)}\right)^2}{8\rho \cdot \sigma^{(i+1)} \cdot \|\mathcal{R}_{\theta^{(i+1)}}(x^{(i)}) - x^{(i)}\|_2^2}\right),$$

where $\sigma^{(i+1)}$ is a subgaussian parameter for $z^{(i+1)} - z^{(i)}$, and a random variable is subgaussian with parameter σ if $\mathbb{P}\{|\cdot| \geq t\} \leq 2\exp(-\frac{t^2}{2\sigma})$ for $t \geq 0$.

Proof. First, observe that

$$\begin{aligned} \|x^{(i)} - z^{(i+1)}\|_2^2 &= \|x^{(i)} - z^{(i)} - (z^{(i+1)} - z^{(i)})\|_2^2 \\ &= \|x^{(i)} - z^{(i)}\|_2^2 + \|z^{(i+1)} - z^{(i)}\|_2^2 - 2\langle x^{(i)} - z^{(i)}, z^{(i+1)} - z^{(i)} \rangle \\ &= \|x^{(i)} - z^{(i)}\|_2^2 + \|z^{(i+1)} - z^{(i)}\|_2^2 - 2\langle z^{(i+1)} - z^{(i)} + \rho(x^{(i)} - \mathcal{R}_{\theta^{(i+1)}}(x^{(i)})), z^{(i+1)} - z^{(i)} \rangle \end{aligned} \quad (\text{S.7})$$

$$= \|x^{(i)} - z^{(i)}\|_2^2 - \|z^{(i+1)} - z^{(i)}\|_2^2 + 2\rho\langle \mathcal{R}_{\theta^{(i+1)}}(x^{(i)}) - x^{(i)}, z^{(i+1)} - z^{(i)} \rangle \quad (\text{S.8})$$

where the inequality (S.7) holds by $x^{(i)} = \rho x^{(i)} - \rho \mathcal{R}_{\theta^{(i+1)}} + z^{(i+1)}$ via (Alg.1.1). We now obtain a probabilistic bound for the third quantity in (S.8) via a concentration inequality. The concentration inequality on the sum of independent zero-mean subgaussian variables (e.g., [9, Thm. 7.27]) yields that for any $t^{(i+1)} \geq 0$

$$\mathbb{P}\left\{\langle \mathcal{R}_{\theta^{(i+1)}}(x^{(i)}) - x^{(i)}, z^{(i+1)} - z^{(i)} \rangle \geq t^{(i+1)}\right\} \leq \exp\left(-\frac{(t^{(i+1)})^2}{2\sigma^{(i+1)}\|\mathcal{R}_{\theta^{(i+1)}}(x^{(i)}) - x^{(i)}\|_2^2}\right) \quad (\text{S.9})$$

where $\sigma^{(i+1)}$ is given as in Lemma S.4. Applying the result (S.9) with $t^{(i+1)} = \frac{1}{2\rho}(\|z^{(i+1)} - z^{(i)}\|_2^2 + \Delta^{(i+1)})$ to the bound (S.8) completes the proofs. \square

Lemma S.4 implies that, given sufficiently large $\Delta^{(i+1)}$, or sufficiently small $\sigma^{(i+1)}$ (e.g., variance for a Gaussian random vector $z^{(i+1)} - z^{(i)}$) or $\|\mathcal{R}_{\theta^{(i+1)}}(x^{(i)}) - x^{(i)}\|_2^2$, bound (12) is satisfied with high probability, for each i . In particular, $\Delta^{(i+1)}$ can be large for the first several layers; if paired operators $(\mathcal{R}_{\theta^{(i+1)}}, \mathcal{R}_{\theta^{(i)}})$ in (Alg.1.1) map their input images to similar output images (e.g., the trained NNs $\mathcal{R}_{\theta^{(i+1)}}$ and $\mathcal{R}_{\theta^{(i)}}$ have good refining capabilities for $x^{(i)}$ and $x^{(i-1)}$), then $\sigma^{(i+1)}$ is small; if the regularization parameter γ in (Alg.1.3) is sufficiently large, then $\|\mathcal{R}_{\theta^{(i+1)}}(x^{(i)}) - x^{(i)}\|_2^2$ is small.

S.3 PROOFS OF PROPOSITION 11

First, we show that $\sum_{i=0}^{\infty} \|x^{(i+1)} - x^{(i)}\|_2^2 < \infty$ for convex and nonconvex $F(x; y, z^{(i+1)})$ cases.

- *Convex $F(x; y, z^{(i+1)})$ case:* Using Assumption 2 and $\{\widetilde{M}^{(i+1)} = M^{(i+1)} : \forall i\}$ for the convex case via (7), we obtain the following results for any \mathcal{X} :

$$\begin{aligned} &F(x^{(i)}; y, z^{(i)}) - F(x^{(i+1)}; y, z^{(i+1)}) + \gamma \Delta^{(i+1)} \\ &\geq F(x^{(i)}; y, z^{(i+1)}) - F(x^{(i+1)}; y, z^{(i+1)}) \end{aligned} \quad (\text{S.10})$$

$$\geq \frac{1}{2} \|x^{(i+1)} - \hat{x}^{(i+1)}\|_{M^{(i+1)}}^2 + (\hat{x}^{(i+1)} - x^{(i)})^T M^{(i+1)} (x^{(i+1)} - \hat{x}^{(i+1)}) \quad (\text{S.11})$$

$$= \frac{1}{2} \|x^{(i+1)} - x^{(i)}\|_{M^{(i+1)}}^2 - \frac{1}{2} \|E^{(i+1)}(x^{(i)} - x^{(i-1)})\|_{M^{(i+1)}}^2 \quad (\text{S.12})$$

$$\geq \frac{1}{2} \|x^{(i+1)} - x^{(i)}\|_{M^{(i+1)}}^2 - \frac{\delta^2}{2} \|x^{(i)} - x^{(i-1)}\|_{M^{(i)}}^2 \quad (\text{S.13})$$

where the inequality (S.10) uses the condition (12) in Assumption 4, the inequality (S.11) is obtained by using the results in [2, Lem. S.1], the equality (S.12) uses the extrapolation formula (Alg.1.2) and the symmetry of $M^{(i+1)}$, the inequality (S.13) holds by Assumption 3.

Summing the inequality of $F(x^{(i)}; y, z^{(i)}) - F(x^{(i+1)}; y, z^{(i+1)}) + \gamma \Delta^{(i+1)}$ in (S.13) over $i = 0, \dots, N_{\text{lyr}} - 1$, we obtain

$$\begin{aligned} F(x^{(0)}; y, z^{(0)}) - F(x^{(N_{\text{lyr}})}; y, z^{(N_{\text{lyr}})}) + \gamma \sum_{i=0}^{N_{\text{lyr}}-1} \Delta^{(i+1)} &\geq \sum_{i=0}^{N_{\text{lyr}}-1} \frac{1}{2} \|x^{(i+1)} - x^{(i)}\|_{M^{(i+1)}}^2 - \frac{\delta^2}{2} \|x^{(i)} - x^{(i-1)}\|_{M^{(i)}}^2 \\ &\geq \sum_{i=0}^{N_{\text{lyr}}-1} \frac{1 - \delta^2}{2} \|x^{(i+1)} - x^{(i)}\|_{M^{(i+1)}}^2 \\ &\geq \sum_{i=0}^{N_{\text{lyr}}-1} \frac{m_{F, \min}(1 - \delta^2)}{2} \|x^{(i+1)} - x^{(i)}\|_2^2 \end{aligned} \quad (\text{S.14})$$

where the inequality (S.14) holds by Assumption 2. Due to the lower boundedness of $F(x; y, z)$ in Assumption 1 and the summability of $\{\Delta^{(i+1)} \geq 0 : \forall i\}$ in Assumption 4, taking $N_{\text{lyr}} \rightarrow \infty$ gives

$$\sum_{i=0}^{\infty} \|x^{(i+1)} - x^{(i)}\|_2^2 < \infty. \quad (\text{S.15})$$

- Nonconvex $F(x; y, z^{(i+1)})$ case: Using Assumption 2, we obtain the following results without assuming that $F(x; y, z^{(i+1)})$ is convex:

$$\begin{aligned} &F(x^{(i)}; y, z^{(i)}) - F(x^{(i+1)}; y, z^{(i+1)}) + \gamma \Delta^{(i+1)} \\ &\geq F(x^{(i)}; y, z^{(i+1)}) - F(x^{(i+1)}; y, z^{(i+1)}) \end{aligned} \quad (\text{S.16})$$

$$\geq \frac{\lambda - 1}{4} \|x^{(i+1)} - x^{(i)}\|_{M^{(i+1)}}^2 - \frac{(\lambda + 1)^2}{\lambda - 1} \|x^{(i)} - \hat{x}_b^{(i+1)}\|_{M^{(i+1)}}^2 \quad (\text{S.17})$$

$$= \frac{\lambda - 1}{4} \|x^{(i+1)} - x^{(i)}\|_{M^{(i+1)}}^2 - \frac{(\lambda + 1)^2}{\lambda - 1} \|E^{(i+1)}(x^{(i)} - x^{(i-1)})\|_{M^{(i+1)}}^2 \quad (\text{S.18})$$

$$\geq \frac{\lambda - 1}{4} \left(\|x^{(i+1)} - x^{(i)}\|_{M^{(i+1)}}^2 - \delta^2 \|x^{(i)} - x^{(i-1)}\|_{M^{(i)}}^2 \right) \quad (\text{S.19})$$

where the inequality (S.16) uses the condition (12) in Assumption 4, the inequality (S.17) use the results in [3, §S.3], the equality (S.18) holds by (Alg.1.2), the inequality (S.19) is obtained by Assumption 3.

Summing the inequality of $F(x^{(i)}; y, z^{(i)}) - F(x^{(i+1)}; y, z^{(i+1)}) + \gamma \Delta^{(i+1)}$ in (S.19) over $i = 0, \dots, N_{\text{lyr}} - 1$, we obtain

$$\begin{aligned} F(x^{(0)}; y, z^{(0)}) - F(x^{(N_{\text{lyr}})}; y, z^{(N_{\text{lyr}})}) + \gamma \cdot \sum_{i=0}^{N_{\text{lyr}}-1} \Delta^{(i+1)} &\geq \sum_{i=0}^{N_{\text{lyr}}-1} \frac{\lambda - 1}{4} \left(\|x^{(i+1)} - x^{(i)}\|_{M^{(i+1)}}^2 - \delta^2 \|x^{(i)} - x^{(i-1)}\|_{M^{(i)}}^2 \right) \\ &\geq \sum_{i=0}^{N_{\text{lyr}}-1} \frac{(\lambda - 1)(1 - \delta^2)}{2} \|x^{(i+1)} - x^{(i)}\|_{M^{(i+1)}}^2 \\ &\geq \sum_{i=0}^{N_{\text{lyr}}-1} \frac{m_{F, \min}(\lambda - 1)(1 - \delta^2)}{2} \|x^{(i+1)} - x^{(i)}\|_2^2, \end{aligned}$$

where we follow the arguments in obtaining (S.14) above. Again, using the lower boundedness of $F(x; y, z)$ and the summability of $\{\Delta^{(i+1)} \geq 0 : \forall i\}$, taking $N_{\text{lyr}} \rightarrow \infty$ gives the result (S.15) for nonconvex $F(x; y, z^{(i+1)})$.

Second, we show that $\sum_{i=0}^{\infty} \|z^{(i+1)} - z^{(i)}\|_2^2 < \infty$. Observe

$$\begin{aligned} \|z^{(i+1)} - z^{(i)}\|_2^2 &= \left\| (1 - \rho)(x^{(i)} - x^{(i-1)}) + \rho(\mathcal{R}_{\theta^{(i+1)}}(x^{(i)}) - \mathcal{R}_{\theta^{(i)}}(x^{(i-1)})) \right\|_2^2 \\ &\leq (1 - \rho) \|x^{(i)} - x^{(i-1)}\|_2^2 + \rho \|\mathcal{R}_{\theta^{(i+1)}}(x^{(i)}) - \mathcal{R}_{\theta^{(i)}}(x^{(i-1)})\|_2^2 \\ &\leq \|x^{(i)} - x^{(i-1)}\|_2^2 + \rho \epsilon^{(i+1)} \end{aligned} \quad (\text{S.20})$$

where the first equality uses the image mapping formula in (Alg.1.1), the first inequality holds by applying Jensen's inequality to the (convex) squared ℓ^2 -norm, the second inequality is obtained by using the asymptotically non-expansiveness of the paired operators $(\mathcal{R}_{\theta^{(i+1)}}, \mathcal{R}_{\theta^{(i)}})$ in Assumption 4. Summing the inequality of $\|z^{(i+1)} - z^{(i)}\|_2^2$ in (S.20) over $i = 0, \dots, N_{\text{lyr}} - 1$, we obtain

$$\sum_{i=0}^{N_{\text{lyr}}-1} \|z^{(i+1)} - z^{(i)}\|_2^2 \leq \sum_{i=0}^{N_{\text{lyr}}-2} \|x^{(i+1)} - x^{(i)}\|_2^2 + \rho \sum_{i=0}^{N_{\text{lyr}}-1} \epsilon^{(i+1)}, \quad (\text{S.21})$$

where we used $x^{(0)} = x^{(-1)}$ as given in Algorithm 1. By taking $N_{\text{lyr}} \rightarrow \infty$ in (S.21), using result (S.15), and the summability of the sequence $\{\epsilon^{(i+1)} : i \geq 0\}$, we obtain

$$\sum_{i=0}^{\infty} \|z^{(i+1)} - z^{(i)}\|_2^2 < \infty. \quad (\text{S.22})$$

Combining the results in (S.15) and (S.22) completes the proofs.

S.4 PROOFS OF THEOREM 12

Let \bar{x} be a limit point of $\{x^{(i)} : i \geq 0\}$ and $\{x^{(i_j)}\}$ be the subsequence converging to \bar{x} . Let \bar{z} be a limit point of $\{z^{(i)} : i \geq 0\}$ and $\{z^{(i_j)}\}$ be the subsequence converging to \bar{z} . The closedness of \mathcal{X} implies that $\bar{x} \in \mathcal{X}$. Using the results in Proposition 11, $\{x^{(i_j+1)}\}$ and $\{z^{(i_j+1)}\}$ also converge to \bar{x} and \bar{z} , respectively. Taking another subsequence if necessary, the subsequence $\{M^{(i_j+1)}\}$ converges to some \bar{M} , since $M^{(i+1)}$ is bounded by Assumption 2. The subsequences $\{\theta^{(i_j+1)}\}$ converge to some $\bar{\theta}$, since $x^{(i_j+1)} \rightarrow \bar{x}$, $z^{(i_j+1)} \rightarrow \bar{z}$, and $\{\theta^{(i+1)}\}$ is bounded via Assumption 4.

Next, we show that the convex proximal minimization (S.23) below is continuous in the sense that the output point $x^{(i_j+1)}$ continuously depends on the input points $\hat{x}^{(i_j+1)}$ and $z^{(i_j+1)}$, and majorization matrix $\widetilde{M}^{(i_j+1)}$:

$$\begin{aligned} x^{(i_j+1)} &= \underset{x \in \mathcal{X}}{\operatorname{argmin}} \langle \nabla F(\hat{x}^{(i_j+1)}; y, z^{(i_j+1)}), x - \hat{x}^{(i_j+1)} \rangle + \frac{1}{2} \|x - \hat{x}^{(i_j+1)}\|_{\widetilde{M}^{(i_j+1)}}^2 \\ &= \operatorname{Prox}_{\mathbb{I}_{\mathcal{X}}}^{\widetilde{M}^{(i_j+1)}} \left(\hat{x}^{(i_j+1)} - (\widetilde{M}^{(i_j+1)})^{-1} \nabla F(\hat{x}^{(i_j+1)}; y, z^{(i_j+1)}) \right). \end{aligned} \quad (\text{S.23})$$

where the proximal mapping operator $\operatorname{Prox}_{\mathbb{I}_{\mathcal{X}}}^{\widetilde{M}^{(i_j+1)}}(\cdot)$ is given as in (2). We consider the two cases of majorization matrices $\{M^{(i+1)}\}$ given in Theorem 12:

- For a sequence of diagonal majorization matrices, i.e., $\{M^{(i+1)} : i \geq 0\}$, one can obtain the continuity of the convex proximal minimization (S.23) with respect to $\hat{x}^{(i_j+1)}$, $z^{(i_j+1)}$, and $\widetilde{M}^{(i_j+1)}$, by extending the existing results in [10, Thm. 2.26], [11] with the separability of (S.23) to element-wise optimization problems.
- For a fixed general majorization matrix, i.e., $M = M^{(i+1)}$, $\forall i$, we obtain that the convex proximal minimization (S.24) below is continuous with respect to the input points $\hat{x}^{(i_j+1)}$ and $z^{(i_j+1)}$:

$$x^{(i_j+1)} = \underset{x \in \mathcal{X}}{\operatorname{argmin}} \langle \nabla F(\hat{x}^{(i_j+1)}; y, z^{(i_j+1)}), x - \hat{x}^{(i_j+1)} \rangle + \frac{1}{2} \|x - \hat{x}^{(i_j+1)}\|_{\widetilde{M}}^2 \quad (\text{S.24})$$

$$\begin{aligned} &= \operatorname{Prox}_{\mathbb{I}_{\mathcal{X}}}^{\widetilde{M}} (\hat{x}^{(i_j+1)} - \widetilde{M}^{-1} \nabla F(\hat{x}^{(i_j+1)}; y, z^{(i_j+1)})) \\ &= (\operatorname{Id} + \widetilde{M}^{-1} \hat{\partial} \mathbb{I}_{\mathcal{X}})^{-1} (\hat{x}^{(i_j+1)} - \widetilde{M}^{-1} \nabla F(\hat{x}^{(i_j+1)}; y, z^{(i_j+1)})) \end{aligned} \quad (\text{S.25})$$

where $\hat{\partial} f(x)$ is the subdifferential of f at x and Id denotes the identity operator, and the proximal mapping of $\mathbb{I}_{\mathcal{X}}$ relative to $\|\cdot\|_{\widetilde{M}}$ is uniquely determined by the resolvent of the operator $\widetilde{M}^{-1} \hat{\partial} \mathbb{I}_{\mathcal{X}}$ in (S.25).

First, we obtain that the operator $\widetilde{M}^{-1} \hat{\partial} \mathbb{I}_{\mathcal{X}}$ is monotone. For a convex extended-valued function $f_e : \mathbb{R}^N \rightarrow \mathbb{R} \cup \{\infty\}$, observe that $\widetilde{M}^{-1} \hat{\partial} f_e$ is a monotone operator:

$$\langle \widetilde{M}^{-1} \hat{\partial} f_e(u) - \widetilde{M}^{-1} \hat{\partial} f_e(v), u - v \rangle = \underbrace{\langle \widetilde{M}^{-1} \widetilde{M} \hat{\partial} f_e(\widetilde{M} \tilde{u}) - \widetilde{M}^{-1} \widetilde{M} \hat{\partial} f_e(\widetilde{M} \tilde{v}), \widetilde{M} \tilde{u} - \widetilde{M} \tilde{v} \rangle}_{=I} \geq 0, \quad \forall u, v, \quad (\text{S.26})$$

where the equality uses the variable change $\{u = \widetilde{M} \tilde{u}, v = \widetilde{M} \tilde{v}\}$, a chain rule of the subdifferential of a composition of a convex extended-valued function and an affine mapping [12, §7], and the symmetry of \widetilde{M} , and the inequality holds because the subdifferential of convex extended-valued function is a monotone operator [13, §4.2]. Because indicator function of a convex set is extended-valued function, the result in (S.26) implies that the operator $\widetilde{M}^{-1} \hat{\partial} \mathbb{I}_{\mathcal{X}}$ is monotone. Second, note that the resolvent of a monotone operator $\widetilde{M}^{-1} \hat{\partial} \mathbb{I}_{\mathcal{X}}$ (with a parameter 1), i.e., $(\operatorname{Id} + \widetilde{M}^{-1} \hat{\partial} \mathbb{I}_{\mathcal{X}})^{-1}$ in (S.25), is nonexpansive [10, §6] and thus continuous. We now obtain that the convex proximal minimization (S.24) is continuous with respect to the input points $\hat{x}^{(i_j+1)}$ and $z^{(i_j+1)}$, because the proximal mapping operator $(\operatorname{Id} + \widetilde{M}^{-1} \hat{\partial} \mathbb{I}_{\mathcal{X}})^{-1}$ in (S.25), the affine mapping \widetilde{M}^{-1} , and $\nabla F(x; y, z)$ are continuous with respect to their input points.

For the two cases above, using the fact that $x^{(i_j+1)} \rightarrow \bar{x}$, $\hat{x}^{(i_j+1)} \rightarrow \bar{x}$, $z^{(i_j+1)} \rightarrow \bar{z}$, and $M^{(i_j+1)} \rightarrow \bar{M}$ (or $\bar{M} = M$ for the $\{M^{(i+1)} = M\}$ case) as $j \rightarrow \infty$, (S.23) becomes

$$\bar{x} = \underset{x \in \mathcal{X}}{\operatorname{argmin}} \langle \nabla F(\bar{x}; y, \bar{z}), x - \bar{x} \rangle + \frac{1}{2} \|x - \bar{x}\|_{\bar{M}}^2. \quad (\text{S.27})$$

Thus, \bar{x} satisfies the first-order optimality condition of $\min_{x \in \mathcal{X}} F(x; y, \bar{z})$:

$$\langle \nabla F(\bar{x}; y, \bar{z}), x - \bar{x} \rangle \geq 0, \quad \text{for any } x \in \mathcal{X},$$

and this completes the proof of the first result.

Next, note that the result in Proposition 11 imply

$$\left\| \mathcal{A}_{\mathcal{R}_{\theta^{(i+1)}}}^{M^{(i+1)}} \left(\begin{bmatrix} x^{(i)} \\ x^{(i-1)} \end{bmatrix} \right) - \begin{bmatrix} x^{(i)} \\ x^{(i-1)} \end{bmatrix} \right\|_2 \rightarrow 0. \quad (\text{S.28})$$

Additionally, note that a function $\mathcal{A}_{\mathcal{R}_{\theta^{(i+1)}}}^{M^{(i+1)}} - I$ is continuous. To see this, observe that the convex proximal mapping in (Alg.1.3) is continuous (see the obtained results above), and $\mathcal{R}_{\theta^{(i+1)}}$ is continuous (see Assumption 4). Combining (S.28), the convergence of $\{M^{(i_j+1)}, \mathcal{R}_{\theta^{(i_j+1)}}\}$, and the continuity of $\mathcal{A}_{\mathcal{R}_{\theta^{(i+1)}}}^{M^{(i+1)}} - I$, we obtain $[\bar{x}^T, \bar{x}^T]^T = \mathcal{A}_{\mathcal{R}_{\bar{\theta}}}^M([\bar{x}^T, \bar{x}^T]^T)$, and this completes the proofs of the second result.

S.5 PROOFS OF COROLLARY 13

To prove the first result, we use proof by contradiction. Suppose that $\text{dist}(x^{(i)}, S) \not\rightarrow 0$. Then there exists $\epsilon > 0$ and a subsequence $\{x^{(i_j)}\}$ such that $\text{dist}(x^{(i_j)}, S) \geq \epsilon, \forall j$. However, the boundedness assumption of $\{x^{(i_j)}\}$ in Corollary 13 implies that there must exist a limit point $\bar{x} \in S$ via Theorem 12. This is a contradiction, and gives the first result (via the result in Proposition 11). Under the isolation point assumption in Corollary 13, using the obtained results, $\|x^{(i+1)} - x^{(i)}\|_2 \rightarrow 0$ (via Proposition 11) and $\text{dist}(x^{(i+1)}, S) \rightarrow 0$, and the following the proofs in [4, Cor. 2.4], we obtain the second result.

S.6 PROOFS OF PROPOSITION 14

We rewrite the updates in Algorithm 2 as follows:

$$\begin{aligned} x^{(i+1)} &= \underset{x \in \mathcal{X}}{\text{argmin}} f(x; y) + \frac{\gamma}{2} \|x - \mathcal{R}_{\theta^{(i+1)}}(x^{(i)})\|_2^2 = \text{Prox}_{f + \mathbb{I}_{\mathcal{X}}}^{\gamma I}(\mathcal{R}_{\theta^{(i+1)}}(x^{(i)})) \\ &= (\text{Id} + \gamma^{-1} \hat{\partial}(f(x; y) + \mathbb{I}_{\mathcal{X}}))^{-1}(\mathcal{R}_{\theta^{(i+1)}}(x^{(i)})) \\ &=: \mathcal{A}^{(i+1)}(x^{(i)}). \end{aligned}$$

We first show that the paired operators $\{\mathcal{A}^{(i+1)}, \mathcal{A}^{(i)}\}$ is asymptotically contractive:

$$\begin{aligned} &\left\| \mathcal{A}^{(i+1)}(u) - \mathcal{A}^{(i)}(v) \right\|_2 \\ &= \left\| (\text{Id} + \gamma^{-1} \hat{\partial}(f(x; y) + \mathbb{I}_{\mathcal{X}}))^{-1}(\mathcal{R}_{\theta^{(i+1)}}(u)) - (\text{Id} + \gamma^{-1} \hat{\partial}(f(x; y) + \mathbb{I}_{\mathcal{X}}))^{-1}(\mathcal{R}_{\theta^{(i)}}(v)) \right\|_2 \\ &\leq \left\| \mathcal{R}_{\theta^{(i+1)}}(u) - \mathcal{R}_{\theta^{(i)}}(v) \right\|_2 \\ &\leq L' \|u - v\|_2 + \epsilon^{(i+1)} \|u - v\|_2, \end{aligned} \quad (\text{S.29})$$

$$\leq L' \|u - v\|_2 + \epsilon^{(i+1)} \|u - v\|_2, \quad (\text{S.30})$$

$\forall u, v$, where the inequality (S.29) holds because the subdifferential of the convex extended-valued function $f(x; y) + \mathbb{I}_{\mathcal{X}}$ (the indicator function of a convex set \mathcal{X} , $\mathbb{I}_{\mathcal{X}}$, is convex, and the sum of the two convex functions, $f(x; y) + \mathbb{I}_{\mathcal{X}}$, is convex) is a monotone operator [13, §4.2], and the resolvent of a monotone relation with a positive parameter, i.e., $(\text{Id} + \gamma^{-1} \hat{\partial}(f(x; y) + \mathbb{I}_{\mathcal{X}}))^{-1}$ with $\gamma^{-1} > 0$, is nonexpansive [13, §6], and the inequality (S.30) holds by $L' < 1$ via the contractiveness of the paired operators $(\mathcal{R}_{\theta^{(i+1)}}, \mathcal{R}_{\theta^{(i)}})$, $\forall i$. Note that the inequality (S.29) does not hold for nonconvex $f(x; y)$ and/or \mathcal{X} . Considering that $L' < 1$, we show that the sequence $\{x^{(i+1)} : i \geq 0\}$ is Cauchy sequence:

$$\begin{aligned} \left\| x^{(i+l)} - x^{(i)} \right\|_2 &= \left\| (x^{(i+l)} - x^{(i+l-1)}) + \dots + (x^{(i+1)} - x^{(i)}) \right\|_2 \\ &\leq \left\| x^{(i+l)} - x^{(i+l-1)} \right\|_2 + \dots + \left\| x^{(i+1)} - x^{(i)} \right\|_2 \\ &\leq (L^{l-1} + \dots + 1) \left\| x^{(i+1)} - x^{(i)} \right\|_2 + (\epsilon^{(i+l)} + \dots + \epsilon^{(i+1)}) \\ &\leq \frac{1}{1-L} \left\| x^{(i+1)} - x^{(i)} \right\|_2 + \sum_{i'=1}^l \epsilon^{(i+i')} \end{aligned}$$

where the second inequality uses the result in (S.30). Since the sequence $\{x^{(i+1)} : i \geq 0\}$ is Cauchy sequence, $\{x^{(i+1)} : i \geq 0\}$ is convergent, and this completes the proofs.

S.6.1 Connection between convolutional training loss (P2) and its patch-based training loss

This section shows some superior properties of the convolutional training loss in (P2) compared to the patch-based training loss in [14], [15], based on the following lemma:

Lemma S.5. *The loss function (P2) for training the residual convolutional autoencoder in (18) is bounded by the patch-based loss function:*

$$\frac{1}{2L} \sum_{l=1}^L \left\| \hat{x}_l^{(i)} - \frac{1}{R} \sum_{k=1}^K d_k \otimes \mathcal{T}_{\alpha_k}(e_k \otimes x_l^{(i)}) \right\|_2^2 \leq \frac{1}{2LR} \sum_{l=1}^L \left\| \hat{X}_l^{(i)} - D\mathcal{T}_{\bar{\alpha}}(EX_l^{(i)}) \right\|_F^2, \quad (\text{S.31})$$

where the residual is defined by $\hat{x}_l^{(i)} := x_l - x_l^{(i)}$, $\{x_l, x_l^{(i)}\}$ are given as in (P2), $\hat{X}_l \in \mathbb{R}^{R \times V_l}$ and $X_l \in \mathbb{R}^{R \times V_l}$ are the l th training data matrices whose columns are V_l vectorized patches extracted from the images \hat{x}_l and x_l (with the circulant boundary condition and the “stride” parameter 1), respectively, $D := [d_1, \dots, d_K] \in \mathbb{C}^{R \times K}$ is a decoding filter matrix, and $E := [e_1^*, \dots, e_K^*]^H \in \mathbb{C}^{K \times R}$ is an encoding filter matrix. Here, the definition of soft-thresholding operator in (6) is generalized by

$$(\mathcal{T}_{\tilde{\alpha}}(u))_k := \begin{cases} u_k - \alpha_k \cdot \text{sign}(u_k), & |u_k| > \alpha_k, \\ 0, & \text{otherwise,} \end{cases} \quad (\text{S.32})$$

for $K = 1, \dots, K$, where $\tilde{\alpha} = [\alpha_1, \dots, \alpha_K]^T$. See other related notations in (18).

Proof. First, we have the following reformulation [3, §S.1]:

$$\begin{bmatrix} e_1 * u \\ \vdots \\ e_K * u \end{bmatrix} = \underbrace{P' \begin{bmatrix} EP_1 \\ \vdots \\ EP_N \end{bmatrix}}_{:= \tilde{E}} u, \quad \forall u, \quad (\text{S.33})$$

where $P' \in \mathbb{C}^{KN \times KN}$ is a permutation matrix, E is defined in Lemma (S.5), and $P_n \in \mathbb{C}^{R \times N}$ is the n th patch extraction operator for $n = 1, \dots, N$. Considering that $\frac{1}{R} \sum_{k=1}^K \text{flip}(e_k^*) \otimes (e_k \otimes u) = \tilde{E}^H \tilde{E} u$ via the definition of \tilde{E} in (S.33) (see also the reformulation technique in [3, §S.1]), we obtain the following reformulation result:

$$\frac{1}{R} \sum_{k=1}^K \text{flip}(e_k^*) \otimes \mathcal{T}_{\alpha_k}(e_k \otimes x_l^{(i)}) = \frac{1}{R} \sum_{n=1}^N P_n^H E^H \mathcal{T}_{\tilde{\alpha}}(EP_n x_l^{(i)}) \quad (\text{S.34})$$

where the soft-thresholding operators $\{\mathcal{T}_{\alpha_k}(\cdot) : \forall k\}$ and $\mathcal{T}_{\tilde{\alpha}}(\cdot)$ are defined in (S.32) and we use the permutation invariance of the thresholding operator $\mathcal{T}_{\alpha}(\cdot)$, i.e., $\mathcal{T}_{\alpha}(P(\cdot)) = P \cdot \mathcal{T}_{\alpha}(\cdot)$ for any α . Finally, we obtain the result in (S.31) as follows:

$$\frac{1}{2L} \sum_{l=1}^L \left\| \hat{x}_l^{(i)} - \frac{1}{R} \sum_{k=1}^K d_k \otimes \mathcal{T}_{\alpha_k}(e_k \otimes x_l^{(i)}) \right\|_2^2 = \frac{1}{2L} \sum_{l=1}^L \left\| \hat{x}_l^{(i)} - \frac{1}{R} \sum_{n=1}^N P_n^H D \mathcal{T}_{\tilde{\alpha}}(EP_n x_l^{(i)}) \right\|_2^2 \quad (\text{S.35})$$

$$= \frac{1}{2L} \sum_{l=1}^L \left\| \frac{1}{R} \sum_{n=1}^N P_n^H P_n \hat{x}_l^{(i)} - \frac{1}{R} \sum_{n=1}^N P_n^H D \mathcal{T}_{\tilde{\alpha}}(EP_n x_l^{(i)}) \right\|_2^2 \quad (\text{S.36})$$

$$= \frac{1}{2LR^2} \sum_{l=1}^L \left\| \sum_{n=1}^N P_n^H \left(\hat{x}_{l,n}^{(i)} - D \mathcal{T}_{\tilde{\alpha}}(Ex_{l,n}^{(i)}) \right) \right\|_2^2$$

$$\leq \frac{1}{2LR} \sum_{l=1}^L \sum_{n=1}^N \left\| \hat{x}_{l,n}^{(i)} - D \mathcal{T}_{\tilde{\alpha}}(Ex_{l,n}^{(i)}) \right\|_2^2 \quad (\text{S.37})$$

$$= \frac{1}{2LR} \sum_{l=1}^L \left\| \hat{X}_l^{(i)} - D \mathcal{T}_{\tilde{\alpha}}(EX_l^{(i)}) \right\|_F^2,$$

where D is defined in Lemma S.5, $\{\hat{x}_{l,n}^{(i)} = P_n \hat{x}_l^{(i)} \in \mathbb{C}^R, x_{l,n}^{(i)} = P_n x_l^{(i)} \in \mathbb{C}^R : n = 1, \dots, N\}$ is a set of extracted patches, the training matrices $\{\hat{X}_l^{(i)}, X_l^{(i)}\}$ are defined by $\hat{X}_l^{(i)} := [\hat{x}_{l,1}^{(i)}, \dots, \hat{x}_{l,N}^{(i)}]$ and $X_l^{(i)} := [x_{l,1}^{(i)}, \dots, x_{l,N}^{(i)}]$. Here, the equality (S.35) uses the result in (S.34), the equality (S.36) holds by $\sum_{n=1}^N P_n^H P_n = R \cdot I$ (for the circulant boundary condition in Lemma S.5), and the inequality (S.37) holds by $\tilde{P} \tilde{P}^H \preceq R \cdot I$ with $\tilde{P} := [P_1^H \dots P_N^H]^H$. \square

Lemma S.5 reveals that when the patch-based training approach extract all the R -size overlapping patches, 1) the corresponding patch-based loss is an upper bound of the convolutional loss (P2); 2) it requires about R -times larger memory than (P2) because $V_l \approx RN_l$ for $x \in \mathbb{R}^{N_l}$ and the boundary condition described in Lemma S.5, $\forall l$; and 3) it misses modeling the patch aggregation process that is inherently modeled in (18) – see that the patch aggregation operator $\sum_{n=1}^N P_n^H(\cdot)_n$ is removed in the inequality (S.37) in the proof of Lemma S.5. In addition, different from the patch-based training approach [14], [15], i.e., training with the function on the right-hand side in (S.31), one can use different sizes of filters $\{e_k, d_k : \forall k\}$ in the convolutional training loss, i.e., the function on the left-hand side in (S.31).

S.7 SUBDIFFERENTIALS OF TRAINING LOSS (P2) WITH RESPECT TO θ

This section provides the subdifferentials of the mini-batch version of training loss (P2), with respect to $\theta = \{d_k, e_k, a_k : k = 1, \dots, K\}$. First, we decompose (P2) as follows:

$$\{d_k^{(i+1)}, \alpha_k^{(i+1)}, e_k^{(i+1)}\} = \underset{\{d_k, \alpha_k, w_k\}}{\text{argmin}} \frac{1}{2L'} \sum_{l=1}^{L'} \left\| \hat{x}_{l,k}^{(i)} - d_k * \mathcal{T}_{\exp(\alpha_k)}(e_k * x_l^{(i)}) \right\|_2^2, \quad (\text{S.38})$$

where L' is the mini-batch size, $\hat{x}_{l,k}^{(i)} := x_l - \sum_{k' \neq k} d_{k'} * \mathcal{T}_{\alpha_{k'}}(e_{k'} * x_l^{(i)}) - x_l^{(i)}$. For simplicity, we drop the filter subscript indices k and layer superscript indices $(\cdot)^{(i)}$ in (S.38) throughout. We shall obtain the gradients of the following function with respect to d , α , and e :

$$g(d, \alpha, e) := \frac{1}{2L'} \sum_{l=1}^{L'} \|\hat{x}_l - d * \mathcal{T}_{\exp(\alpha)}(e * x_l)\|_2^2. \quad (\text{S.39})$$

S.7.1 Subdifferential of $g(d, \alpha, e)$ in (S.39) with respect to d

We first rewrite the loss function $g(d, \alpha, e)$ in (S.39) as follows:

$$g(d, \alpha, e) = \frac{1}{2L'} \sum_{l=1}^{L'} \|\hat{x}_l - Z_l d\|_2^2, \quad (\text{S.40})$$

$$Z_l := [\Pi^0 \mathcal{T}_{\exp(\alpha)}(e * x_l), \dots, \Pi^{R-1} \mathcal{T}_{\exp(\alpha)}(e * x_l)] \in \mathbb{C}^{N \times R} \quad (\text{S.41})$$

where $\Pi := \begin{bmatrix} 0 & I_{N-1} \\ 1 & 0 \end{bmatrix} \in \mathbb{C}^{N \times N}$ is the circular shift operator [16] and $(\cdot)^r$ denotes the matrix product of its r copies. We consider a circular boundary condition to simplify the presentation of $\{Z_l\}$ in (S.41), but our result below holds for a general boundary condition with only minor modifications of $\{Z_l\}$ as done in [3, §4-A]. The gradient of $g(d, \alpha, e)$ in (S.40) with respect to d is given by

$$\nabla_d g(d, \alpha, e) = \hat{\partial}_d g(d, \alpha, e) = \frac{1}{L'} \sum_{l=1}^{L'} Z_l^H (Z_l d - \hat{x}_l).$$

Using the the column-wise structure of Z_l defined in (S.41), the product between the matrix Z_l^H and the vector $Z_l d - \hat{x}_l$ can be efficiently performed by using multiple inner products, without storing $Z_l^H, \forall l$.

S.7.2 Subdifferential of $g(d, \alpha, e)$ in (S.39) with respect to α

We first rewrite the loss function $g(d, \alpha, e)$ in (S.39) as follows:

$$g(d, \alpha, e) = \frac{1}{2L'} \sum_{l=1}^{L'} \|\hat{x}_l - \Psi \mathcal{T}_{\exp(\alpha)}(e * x_l)\|_2^2, \quad (\text{S.42})$$

$$\Psi x := d * x, \quad (\text{S.43})$$

where $\Psi \in \mathbb{C}^{N \times N}$ is a convolution matrix. Observe that $g(d, \alpha, e)$ in (S.42) can be rewritten by

$$\begin{aligned} g(d, \alpha, e) &= \frac{1}{2L'} \sum_{l=1}^{L'} \sum_{m=1}^N \left| (\hat{x}_l)_m - \sum_{n=1}^{N'} \Psi_{m,n} ((e * x_l)_n - \exp(\alpha) \cdot \text{sign}(e * x_l)_n) \mathbb{1}_{|(e * x_l)_n| > \exp(\alpha)} \right|^2 \\ &= \frac{1}{2L'} \sum_{l=1}^{L'} \sum_{m=1}^N \left| (\hat{x}_l)_m - \sum_{n=1}^{N'} \Psi_{m,n} (e * x_l)_n \mathbb{1}_{|(e * x_l)_n| > \exp(\alpha)} - \exp(\alpha) \cdot \sum_{n=1}^{N'} \Psi_{m,n} \text{sign}(e * x_l)_n \mathbb{1}_{|(e * x_l)_n| > \exp(\alpha)} \right|^2, \end{aligned}$$

where the indicator function $\mathbb{1}_{\mathcal{V}}$ returns 1, if event \mathcal{V} occurs, and 0 otherwise. Using this reformulation and the definition (S.43), we obtain the subdifferential of $g(d, \alpha, e)$ in (S.42) with respect to α :

$$\begin{aligned} \hat{\partial}_\alpha g(d, \alpha, e) &= \frac{-\exp(\alpha)}{2L'} \sum_{l=1}^{L'} \sum_{m=1}^N (c_l)_m^* \cdot (\hat{x}_l - \Psi \mathcal{T}_\alpha(e * x_l))_m + (c_l)_m \cdot (\hat{x}_l - \Psi \mathcal{T}_\alpha(e * x_l))_m^* \\ &= \frac{-\exp(\alpha)}{L'} \sum_{l=1}^{L'} \sum_{m=1}^N \text{Re}\{(\hat{x}_l - d * \mathcal{T}_\alpha(e * x_l))_m \cdot (c_l)_m^*\} \\ &= \frac{-\exp(\alpha)}{L'} \sum_{l=1}^{L'} \text{Re}\langle \hat{x}_l - d * \mathcal{T}_\alpha(e * x_l), d * ((e * x_l) \odot \mathbb{1}_{|e * x_l| > \exp(\alpha)}) \rangle, \\ (c_l)_m &= \sum_{n=1}^N \Psi_{m,n} \cdot \text{sign}(e * x_l)_n \cdot \mathbb{1}_{|(e * x_l)_n| > \exp(\alpha)} = (d * ((e * x_l) \odot \mathbb{1}_{|e * x_l| > \exp(\alpha)}))_m, \end{aligned}$$

by using $(u - \alpha v)^*(u - \alpha v) = (u^* - \alpha v^*)(u - \alpha v)$ with $\alpha \in \mathbb{R}$ and $u, v \in \mathbb{C}$.

S.7.3 Subdifferential of $g(d, \alpha, e)$ in (S.39) with respect to e : Real-valued case

We first rewrite the loss function $g(d, \alpha, e)$ in (S.39) as follows:

$$g(d, \alpha, e) = \frac{1}{2L'} \sum_{l=1}^{L'} \|\hat{x}_l - \Psi \mathcal{T}_{\exp(\alpha)}(X_l e)\|_2^2, \quad (\text{S.44})$$

$$X_l := [\Pi^0 x_l, \dots, \Pi^{R-1} x_l] \in \mathbb{R}^{N \times R}, \quad (\text{S.45})$$

where $\Psi \in \mathbb{R}^{N \times N}$ and $\Pi^r \in \mathbb{R}^{N \times N}$ are given as in (S.43) and (S.41), respectively. Observe that $g(d, \alpha, e)$ in (S.44) can be rewritten by

$$g(d, \alpha, e) = \frac{1}{2L'} \sum_{l=1}^{L'} \sum_{m=1}^N \left((\hat{x}_l)_m - \sum_{n=1}^N \Psi_{m,n} \mathcal{T}_{\exp(\alpha)} \left(\sum_{r=1}^R (X_l)_{n,r} e_r \right) \right)^2$$

and

$$\hat{\partial}_u \mathcal{T}_\alpha(u) = \begin{cases} 1, & |u| > \alpha, \\ 0, & \text{otherwise.} \end{cases}$$

Using these observations and the definition (S.43), we obtain the subdifferential of $g(d, \alpha, e)$ in (S.44) with respect to e :

$$\begin{aligned} \hat{\partial}_{e_r}(d, \alpha, e) &= \frac{-1}{L'} \sum_{l=1}^{L'} \sum_{m=1}^N \left((\hat{x}_l)_m - \sum_{n=1}^N \Psi_{m,n} \mathcal{T}_{\exp(\alpha)} \left(\sum_{r=1}^R (X_l)_{n,r} e_r \right) \right) \cdot \sum_{n=1}^N \Psi_{m,n} \mathbb{1}_{|(X_l e)_n| > \exp(\alpha)} \cdot (X_l)_{n,r} \\ &= \frac{-1}{L'} \sum_{l=1}^{L'} \sum_{m=1}^N (\hat{x}_l - \Psi \mathcal{T}_{\exp(\alpha)}(X_l e))_m \cdot \left(\Psi (\Pi^{r-1} x_l \odot \mathbb{1}_{|X_l e| > \exp(\alpha)}) \right)_m \\ &= \frac{-1}{L'} \sum_{l=1}^{L'} (\hat{x}_l - d * \mathcal{T}_{\exp(\alpha)}(e * x_l))^T \left(d * (\Pi^{r-1} x_l \odot \mathbb{1}_{|e * x_l| > \exp(\alpha)}) \right), \quad r = 1, \dots, R. \end{aligned}$$

S.8 DETAILS OF EXPERIMENTAL SETUP

S.8.1 Majorization matrix designs for quadratic data-fit

For (real-valued) quadratic data-fit $f(x; y)$ in the form of $\frac{1}{2} \|y - Ax\|_W^2$, if a majorization matrix M exists such that $A^H W A \preceq M$, it is straightforward to verify that the gradient of quadratic data-fit $f(x; y)$ satisfies the M -Lipchitz continuity in Definition 1, i.e.,

$$\|\nabla f(u; y) - \nabla f(v; y)\|_{M^{-1}} = \|A^H W A u - A^H W A v\|_{M^{-1}} \leq \|u - v\|_M^2, \quad \forall u, v \in \mathbb{R}^N.$$

because the assumption $A^T W A \preceq M \Leftrightarrow M^{-1/2} A^T W A M^{-1/2} \preceq I$ implies that the eigenspectrum of $M^{-1/2} A^T W A M^{-1/2}$ lies in the interval $[0, 1]$, and gives the following result:

$$(M^{-1/2} A^T W A M^{-1/2})^2 \preceq I \Leftrightarrow (A^T W A) M^{-1} (A^T W A) \preceq M.$$

Next, we review a useful lemma in designing majorization matrices for a wide class of quadratic data-fit $f(x; y)$:

Lemma S.6 ([2, Lem. S.3]). *For a (possibly complex-valued) matrix A and a diagonal matrix W with non-negative entries, $A^H W A \preceq \text{diag}(|A^H|W|A|1)$, where $|A|$ denotes the matrix consisting of the absolute values of the elements of A .*

S.8.2 Parameters for MBIR optimization models: Sparse-view CT reconstruction

For MBIR model using EP regularization, we combined a EP regularizer $\sum_{n=1}^N \sum_{n' \in \mathcal{N}_n} \iota_n \iota_{n'} \varphi(x_n - x_{n'})$ and the data-fit $f(x; y)$ in §4.1.1, where \mathcal{N}_n is the set of indices of the neighborhood, ι_n and $\iota_{n'}$ are parameters that encourage uniform noise [17], and $\varphi(\cdot)$ is the Lange penalty function, i.e., $\varphi(t) = \delta^2(|t/\delta| - \log(1 + |t/\delta|))$, with $\delta = 10$ in HU. We chose the regularization parameter (e.g., γ in (P0)) as $2^{15.5}$. We ran the relaxed linearized augmented Lagrangian method [18] with 100 iterations and 12 ordered-subsets, and initialized the EP MBIR algorithms with a conventional FBP method using a Hanning window.

For MBIR model using a learned convolutional regularizer [6, (P2)], we trained convolutional regularizer with filters of $\{h_k \in \mathbb{R}^R : R = K = 7^2\}$ via CAOL [3] in an unsupervised training manner; see training details in [3]. The regularization parameters (e.g., γ in (1)) were selected by applying the spectral radius based selection scheme in §3.2 with the desired factor $\chi^* = 167.64$. We selected the spatial-strength-controlling hard-thresholding parameter (i.e., α' in [6, (P2)]) as follows: for Test samples #1–2, we chose it is as 10^{-10} and 6^{-11} , respectively. We initialized the MBIR model using a learned regularizer with the EP MBIR results obtained above. We terminated the iterations if the relative error stopping criterion (e.g., [2, (44)]) is met before reaching the maximum number of iterations. We set the tolerance value as 10^{-13} and the maximum number of iterations to 4×10^3 .

S.8.3 Parameters for MBIR optimization models: LF photography using a focal stack

For MBIR model using 4D EP regularization, we combined a 4D EP regularizer $\sum_{n=1}^N \sum_{n' \in \mathcal{N}_n} \varphi(x_n - x_{n'})$ and the data-fit $f(x; y)$ in §4.1.2, where \mathcal{N}_n is the set of indices of the 4D neighborhood, and $\varphi(\cdot)$ is the hyperbola penalty function, i.e., $\varphi(t) = \delta^2(\sqrt{1 + |t/\delta|^2} - 1)$. We selected the hyperbola function parameter δ and regularization parameter (e.g., γ in (P0)) as follows: for Test samples #1–3, we chose them as $\{\delta = 10^{-4}, \gamma = 10^3\}$, $\{\delta = 10^{-1}, \gamma = 10^7\}$, and $\{\delta = 10^{-1}, \gamma = 5 \times 10^3\}$, respectively. We ran the conjugate gradient method with 100 iterations, and initialized the 4D EP MBIR algorithms with $y^T A$ rescaled in the interval $[0, 1]$.

S.8.4 Reconstruction accuracy and depth estimation accuracy of different MBIR methods

This section provides reconstruction accuracy numerics of different MBIR methods in sparse-view CT reconstruction and LF photography using a focal stack, and reports the SPO depth estimation [19] accuracy numerics on reconstructed LFs from different MBIR methods:

TABLE S.1
RMSE (HU) of different CT MBIR methods
(fan-beam geometry with 12.5% projections views and 10^5 incident photons)

	(a) FBP	(b) EP reg.	(c) Learned convolutional reg. [3], [6], $\{R=K=7^2\}$	(d) Momentum-Net, (18) w/ $\{R=K=7^2\}$	(e) Momentum-Net , (18) w/ $\{R=7^2, K=9^2\}$
Test #1	82.8	40.8	35.2	21.3	20.9
Test #2	74.9	38.5	34.5	20.4	18.3

TABLE S.2
PSNR (dB) of different LF MBIR methods
(LF photography systems with $C=5$ detectors obtain a focal stack of LFs consisting of $S=81$ sub-aperture images)

	(a) $A^T y$	(b) 4D EP reg.	(c) Momentum-Net [†]
Test #1	16.4	32.0	35.8
Test #2	21.1	28.1	30.7
Test #3	21.6	28.1	30.9

[†]Each layer of Momentum-Net used an epipolar-domain denoiser in the form of (18) with $\{R=5^2, K=32\}$. See details in §4.2.1.

TABLE S.3
RMSE (in 10^{-2} , m) of estimated depth from reconstructed LFs with different LF MBIR methods
(LF photography systems with $C=5$ detectors obtain a focal stack of LFs consisting of $S=81$ sub-aperture images)

	(a) Ground truth LF	(b) Reconstructed LF by $A^T y$	(c) Reconstructed LF by 4D EP reg.	(d) Reconstructed LF by Momentum-Net [†]
Test #1	4.7	41.0	13.8	8.0
Test #2	30.5	117.6	39.5	34.6
Test #3	n/a [‡]	n/a [‡]	n/a [‡]	n/a [‡]

SPO depth estimation [19] was applied to reconstructed LFs.

[†]Each layer of Momentum-Net used an epipolar-domain denoiser in the form of (18) with $\{R=5^2, K=32\}$. See details in §4.2.1.

[‡]The ground truth depth map for Test sample #3 does not exist in the LF dataset [20].

REFERENCES

- [1] I. Y. Chun, Z. Huang, H. Lim, and J. A. Fessler, “Momentum-Net: Fast and convergent iterative neural network for inverse problems,” submitted, Jul. 2019.
- [2] I. Y. Chun and J. A. Fessler, “Convolutional dictionary learning: Acceleration and convergence,” *IEEE Trans. Image Process.*, vol. 27, no. 4, pp. 1697–1712, Apr. 2018.
- [3] —, “Convolutional analysis operator learning: Acceleration and convergence,” submitted, Jan. 2019. [Online]. Available: <http://arxiv.org/abs/1802.05584>
- [4] Y. Xu and W. Yin, “A block coordinate descent method for regularized multiconvex optimization with applications to nonnegative tensor factorization and completion,” *SIAM J. Imaging Sci.*, vol. 6, no. 3, pp. 1758–1789, Sep. 2013.
- [5] —, “A globally convergent algorithm for nonconvex optimization based on block coordinate update,” *J. Sci. Comput.*, vol. 72, no. 2, pp. 700–734, Aug. 2017.
- [6] I. Y. Chun and J. A. Fessler, “Convolutional analysis operator learning: Application to sparse-view CT,” in *Proc. Asilomar Conf. on Signals, Syst., and Comput.*, Pacific Grove, CA, Oct. 2018, pp. 1631–1635.
- [7] Y. Nesterov, “Gradient methods for minimizing composite functions,” *Math. Program.*, vol. 140, no. 1, pp. 125–161, Aug. 2013.
- [8] A. Beck and M. Teboulle, “A fast iterative shrinkage-thresholding algorithm for linear inverse problems,” *SIAM J. Imaging Sci.*, vol. 2, no. 1, pp. 183–202, Mar. 2009.
- [9] S. Foucart and H. Rauhut, *A mathematical introduction to compressive sensing*. New York, NY: Springer, 2013.
- [10] R. T. Rockafellar and R. J.-B. Wets, *Variational analysis*. Berlin: Springer Verlag, 2009, vol. 317.

- [11] R. T. Rockafellar, "Monotone operators and the proximal point algorithm," *SIAM J. Control Optim.*, vol. 14, no. 5, pp. 877–898, Aug. 1976.
- [12] B. S. Mordukhovich and N. M. Nam, "Geometric approach to convex subdifferential calculus," *Optimization*, vol. 66, no. 6, pp. 839–873, 2017.
- [13] E. K. Ryu and S. Boyd, "Primer on monotone operator methods," *Appl. Comput. Math.*, vol. 15, no. 1, pp. 3–43, Jan. 2016.
- [14] I. Y. Chun and J. A. Fessler, "Deep BCD-net using identical encoding-decoding CNN structures for iterative image recovery," in *Proc. IEEE IVMSP Workshop*, Zagori, Greece, Jun. 2018, pp. 1–5.
- [15] I. Y. Chun, X. Zheng, Y. Long, and J. A. Fessler, "BCD-Net for low-dose CT reconstruction: Acceleration, convergence, and generalization," in *Proc. Med. Image Comput. and Computer Assist. Inte. (MICCAI)* (accepted), Jul. 2019.
- [16] I. Y. Chun, D. Hong, B. Adcock, and J. A. Fessler, "Convolutional analysis operator learning: Dependence on training data and compressed sensing recovery guarantees," to appear in *IEEE Signal Process. Lett.*, Jun. 2019. [Online]. Available: <http://arxiv.org/abs/1902.08267>
- [17] J. H. Cho and J. A. Fessler, "Regularization designs for uniform spatial resolution and noise properties in statistical image reconstruction for 3-D X-ray CT," *IEEE Trans. Med. Imag.*, vol. 34, no. 2, pp. 678–689, Feb. 2015.
- [18] H. Nien and J. A. Fessler, "Relaxed linearized algorithms for faster X-ray CT image reconstruction," *IEEE Trans. Med. Imag.*, vol. 35, no. 4, pp. 1090–1098, Apr. 2016.
- [19] S. Zhang, H. Sheng, C. Li, J. Zhang, and Z. Xiong, "Robust depth estimation for light field via spinning parallelogram operator," *Comput. Vis. Image Und.*, vol. 145, pp. 148–159, Apr. 2016.
- [20] K. Honauer, O. Johannsen, D. Kondermann, and B. Goldluecke, "A dataset and evaluation methodology for depth estimation on 4D light fields," in *Proc. ACCV*, Taipei, Taiwan, Nov. 2016, pp. 19–34.